FINAL REPORT

CFD CODE EVALUATION FOR INTERNAL FLOW MODELING

(NAG 8–095)

T.J. CHUNG

Department of Mechanical Engineering
The University of Alabama in Huntsville
Huntsville, AL 35899

Submitted to

National Aeronautics and Space Administration
Marshall Space Flight Center

December 1990

SUMMARY

This report contains the research on the CFD code evaluation with emphasis on supercomputing in reacting flows. Advantages of unstructured grids, multigrids, adaptive methods, improved flow solvers, vector processing, parallel processing, reduction of memory requirements are discussed. As examples, we include applications of supercomputing to reacting flow Navier–Stokes equations including shock waves and turbulence and combustion instability problems associated with solid and liquid propellants. This report does not include evaluation of codes developed by other organizations. Instead, the basic criteria for accuracy and efficiency have been established, and some applications on rocket combustion have been made. Research toward an ultimate goal, the most accurate and efficient CFD code, is in progress and will continue for years to come.

TABLE OF CONTENTS

1. INTRODUCTION

The literature on computational fluid dynamics is preponderant, interwoven with success and failure. Stable and accurate solutions are attributed to low Reynolds number, low Mach number, and low Pechlet number. As these numbers increase, however, we encounter convection of flow to be critical, resulting in turbulence for large Reynolds numbers, and thermal discontinuities for large Mach numbers, and thermal discontinuities for large Pechlet numbers. These physical phenomena lead to unstable, nonconvergent, and inaccurate solutions.

It is, therefore, important to devise the most efficient schemes to obtain stable, convergent, and accurate solutions for difficult flow situations such as those occurring in propulsion systems and the space shuttle main engine in particular. Many such attempts have been reported in the open literature for the past two decades. No consolidated efforts, however, have been made to evaluate all of the available codes to date. Each code has merits and demerits. Often defects are buried and unknown to the user, a cause for great frustration.

If the fastest time–scale in the system of equations is not physically relevant for the problem at hand, much lower modes carry the physical information as exhibited in implicit methods [1–4]. A typical example is the viscous flow past an airfoil where the speed of sound limitation in the cells covering the boundary layer would impose severe time step restrictions for an explicit scheme without achieving any further accuracy. Similarly, widely disparate time and length scales which occur in turbulent flows or highly convective flows will require special treatments.

The use of the finite difference method (FDM), both implicit (e.g., Beam and Warming [3]) and explicit (e.g., McCormick [5]) has been successfully applied to aerodynamic problems. Initially, most applications were for external flow problems. More current applications have shown these methods to be useful also for internal flow problems.

Other approaches which are becoming useful are the finite element methods (FEM) using unstructured grids. Computational difficulties involved in flows with high Reynolds numbers, Mach numbers, and Pechlet numbers are treated in FEM [7] in a manner similar to FDM [8] in some cases, but there are unique features of FEM which warrant further investigation. These include efficient treatments of widely disparate length and time scales in convection, shocks, turbulence, and reacting fluids through multigrid adaptive methods in supercomputing with vector and parallel processing.

For many years CFD grew around FDM as they were simple to understand and code, easy to vectorize, in structured grids for simple geometries. However, as computers became bigger and faster, attempts were made to simulate more and more complex flow domains, and it appeared that unstructured grids may be flexible enough to describe these domains. It was at this point in time that unstructured grids with finite elements – a natural way of discretizing operators on them – entered the scene of CFD. Since then, unstructured grids have been used in FEM together with domain splitting [9] and adaptive refinement [10, 11]. Many more developments, however, are still needed in order to transform FEM into efficient engineering tools for CFD.

The Beam and Warming scheme, in its basic form, can be rewritten for unstructured grids. However, the approximate factorization used for structured grids must be replaced by the solution of a full matrix [4]. The solution of full matrices can only be attacked via unstructured multigrid methods. MacCormick's implicit two–step procedure makes heavy use of upwind–differencing, thus always assuming a structured grid, and for this reason cannot be used in the present context. A barely implicit scheme [6], unlike the two former methods, treats only the sound waves implicitly by solving a modified Poisson equation for the pressure. Therefore, instead of solving five coupled equations in 3–D for the Euler equations, only one needs to be solved. The resulting Poisson equation is again solved via unstructured multigrid methods.

We shall discuss unstructured grids, multigrid methods, adaptive methods, improved flow solvers, supercomputer utilization, applications to turbulent reacting flows, solutions using finite element techniques, and applications toward combustion instability in the following sections.

2. UNSTRUCTURED GRIDS

The accurate representation of arbitrary domains represents perhaps one of the most challenging problems in CFD. The magnitude of this problems does not become apparent in two dimensions because only a few singular points usually appear in the field (and may be ignored) and, due to the computer capacity now available, a gross overmeshing in certain regions of the domain can still be handled.

However, anyone trying to mesh complicated geometries in three dimensions with structured grids will encounter singular lines, and the unavoidable cost of overmeshing can no longer be ignored (the result being coarse grids).

It is by now generally accepted that unstructured grids are capable of describing accurately complicated geometries in 3–D better than structured grids. Two different levels of unstructuring are possible.

(1) Macro–unstructuring, where blocks of structured grids are combined to form an unstructured grid (these are so–called zonal methods).

(2) Micro–unstructuring, in which case the point and element distribution can, in principle, be random.

Although macro–unstructuring is being actively pursued by several groups [12–14], the inherent structure at the difference–level precludes simple mesh refinement by local enrichment (which destroys the grid structure). Major problems will also appear when the region to be refined/enriched crosses zone–boundaries. Micro–unstructuring does not have these inherent limitations, but does have disadvantages such as programming difficulties and large storage requirements.

However great the disadvantages of micro–unstructured grids may appear, the advantages these grids offer by far outweigh them. For example, (1) any geometry can be described [15,16], (2) mesh refinement either by movement [17–20], enrichment [21–31], or remeshing [32] presents no problems, and (3) domain splitting [9, 46] for transient problems can easily be performed. Recently, Jameson [16] also presented results using unstructured grids, and this alone may indicate a turning point in the development of CFD.

The fast generation of grids for arbitrary domains in three dimensions has been the focus of much research in recent years. A variety of different approaches have been investigated. The most promising seems to be: the macro–element approach [34, 35], Watson's algorithm [36–41] for Voronoi tesselations combined with a point distribution obtained by superposition of local (structured) grids [16], modified octree [42], on an advancing front [32,43,44], and from a regular background [45]. All of them have advantages and disadvantages, and none has been fast and simple enough to generate efficiently grids of the size needed in 3–D aerodynamic simulations. Grid generation for unstructured grids in 3–D has been pursued for only a few years by a few individuals.

Based on the current state–of–the–art, the following conclusions are drawn:

- Partially unstructured grids (the macro–element approach [34,35]) do not offer enough flexibility to serve as the basis of a general mesh generator for complex domains, unless some major breakthrough in interactive graphical display is achieved.
- Use of regular background grids [45] is not advisable for unbounded problems, as element stretching and point clustering are not accommodated easily. However, this technique may prove useful for internal flow problems.
- The generation of points via superposition of local grids (mapping) [16] seems to offer the greatest flexibility at minimal cost. The point distribution for each local grid is obtained algebraically and is therefore very fast. The grids are chosen from a menu of possible local grids.

- The tetrahedrization of the domain via Watson's algorithm [36,37], as employed and modified in [16,18,41], is not advisable as this algorithm is suboptimal, requiring $O(N^{1.5})$ operations, and the treatment of voids in the fluid domain becomes both grid logic and CPU–intensive.
- It seems attractive to pursue the element generation of [44], combining it with a fast neighbor finder [46–48].

3. MULTIGRID METHODS

Multigrid methods combine two very desirable properties in that they require the least amount of operations to solve large problems (O (N logN) for a problems with N grid points) and their storage requirements are also low (again, O(N logN) for a problem with N grid points). In 1985, Löhner and Morgan [46, 49] advanced the concept of unstructured multigrid methods. It became clear that as the finest grid had to be unstructured in order to accurately represent the domain, it could not be obtained by subdivision of some coarser grid. Instead, a set of unrelated coarsening grids had to be employed. The reason why multigrid methods should still work on sets of unrelated, unstructured grids – the same argument on which all multigrid methods base the convergence rate estimates – is that if the residual is smooth, any coarser grid should be able to "see" it. In all other aspects, the theory follows exactly the lines of traditional multigrid methods [50,51].

The solution of elliptic PDE's via multigrid methods is by now well understood, and rigorous theoretical estimates for the expected convergence rates are available [51]. The main difficulty that can appear for unstructured grid lies in the construction of efficient smoothers, as neither line– nor plane– relaxation are possible. If Jacobi–type smoothers are employed, the convergence rate of the highest modes can degrade seriously for highly stretched elements or diffusion tensors in which one direction is dominant [52]. Three different smoothing schemes are known to avoid this problem:

(1) Use of supersteps: here, the simple Jacobi–smoothing is over– and under–relaxed alternately using a Chebyshev–series. Although not advisable for highly stretched grids, e.g., stretching beyond 1:100, this method is very simple to code and lends itself easily to vectorization.

(2) Solution of local problems: instead of a tighter coupling of modes via line– or plane–relaxation, groups of elements are relaxed, producing the desired effect [53]. This method is applicable in all cases, but may not be vectorizable and also requires some software–overhead.

(3) Element–by–element preconditioning: although the transfer of information in the element–by–element iterative solver [54,55] is local in nature and therefore cannot compete with multigrid methods, this scheme may prove useful as a preconditioner. The compression of the eigenvalue spectrum is achieved by multiplying the system matrix with the (local) element–matrix inverses where appropriate. Vectorization of this type of method should also be investigated further.

For the hyperbolic case, the theory of multigrid methods is still far from complete. Although Ni's method [56–59] has been shown to work well in many cases, Jameson's multigrid solver [60,61] seems to emerge as the more reliable. This is to be expected, since the Runge–Kutta time stepping allows more possibilities for choosing appropriate "damping–sequences" than the Lax–Wendroff schemes. The combination of unstructured multigrid methods with Runge–Kutta time stepping for the Euler equations also appears to be useful [62,63].

4. ADAPTIVE METHODS

In convection–dominated problems, discontinuities or regions with sharp gradients will usually appear. The regions in which the flow variables vary abruptly are usually small and are surrounded by large portions of the field in which the flow varies smoothly. Therefore, it is attractive to locally and adaptively refine the mesh where needed until a

preset tolerance for the error has been achieved. Because of the obvious advantages of adaptive refinement, this field is currently receiving increased attention in the literature [10,11]. Any adaptive refinement scheme consists of three different stages: determining what we want to achieve by refining the grid, developing an error indicator/estimator to detect the regions to be refined, and a refinement strategy such as movement, enrichment, or remeshing. There are three specific directions to be considered:

(a) Typically, one aims to have an equidistribution of the "error" throughout the grid [10,11,51–63].

(b) Whole families of error indicators based on different concepts have been shown to be useful. Among the most popular are those based on the change of some "indicator variable" (e.g., entropy [27] or Mach number [20]), those based on interpolation theory estimates [18, 21–26,64,65], and the indicators based on Richardson extrapolation [66].

(c) For the accurate resolution of the flowfields at or near discontinuities, P–enrichment does not seem to be attractive (besides, P–enrichment implies a considerable increase in software complexity). However, it may prove useful for boundary layers, where an essentially smooth flowfield needs to be resolved.

Although further research on more reliable error indicators [65] is needed, the directional refinement advanced in [31] appears to be satisfactory. It is based on the observation that in most flowfields the regions that ought to be refined are of lower dimensionality than the physical space in which the solution is sought. Therefore, if thin, elongated elements parallel to those discontinuities could be generated during the adaptive refinement process, considerable savings in CPU and storage would be realized without sacrificing accuracy.

The first algorithm devised for this purpose was based on mesh enrichment [31], and turned out to be storage, CPU, and software intensive. Since then, Palmerio and Dervieux [20] have tried to incorporate this concept into a mesh movement framework, while Peraire

et al, [32], have advanced the concept of refinement by remeshing. This last concept represents a new and powerful refinement strategy, combining in a very elegant way the advantages of mesh enrichment (such as versatility by the introduction of points and a coarse initial grid for steady state problems) and mesh movement (which produces the desired element shapes near shocks). If it proves useful in 3–D (the search–problem needs to be addressed here), it may completely replace movement and enrichment as refinement strategies. Another major area of applications for fast remeshing algorithms is given by 3–D Free–Lagrange Methods [66], where restructuring of the grid currently represents a major problem. Remeshing would be an ideal solution in this case.

When solving transient problems in which only a few discontinuities appear, adaptive refinement can also be useful in reducing storage and CPU requirements. However, in comparison to steady state problems, further constraints need to be placed on the refinement algorithms in order to realize significant savings:

(a) As the grid adaptation has to be performed many times, the adaptation algorithm must be fast, and therefore must lend itself to vectorization/parallelization.

(b) As the grid adaptation process becomes an integral part of any code, the algorithm should not be storage intensive.

(c) As the feature that has been refined may pass again (e.g., a shock reflection), the original grid should be recovered after the feature has passed.

Of course, directional remeshing or even movement could be incorporated for those cases in which the discontinuities are fairly straight (for curved shocks that interact with each other, only classic h–enrichment will yield acceptable solutions), but the interpolation problem must be solved (otherwise the shock–speeds will be wrong). Another potential problem may arise due to the (apparent) non–vectorizability of the remeshing algorithm. Obviously, this whole topic of adaptive refinement for transient problems represents one of the most difficult ones in CFD; many further innovations are expected.

5. IMPROVED FLOW SOLVERS

For unstructured grids, the extension of schemes from 1–D to 2–D/3–D cannot be performed by operator splitting. This means that only schemes that are truly multi–dimensional in nature can be used. Toward this end, Petrov–Galerkin methods [67], the flux corrected transport (FCT) algorithms, and those schemes generalized to multi–dimensional problems [71–74] appear to be most suitable.

The idea behind FCT is to combine a high order scheme with a low order scheme in such a way that in regions where the variables under consideration vary smoothly, the high order scheme is employed, whereas the low order scheme is favored in those regions where the variables vary abruptly. In this scheme, no nonphysical over/undershoots are created.

It is at this point that a further constraint, given by the conservation equations themselves, must be taken into account: strict conservation on the discrete level should be maintained. The simplest way to guarantee this for the node–centered schemes considered here is by constructing schemes for which the sum of the contributions of each individual element (cell) to its surrounding nodes vanishes, i.e., "all that comes in goes out". This means that the limiting will be carried out in elements (cells).

There are several aspects in FCT worthy of mention:

(a) For systems of equations, no obvious or natural way of limiting has been identified yet. Several possibilities have been explored, among them (for the Euler equations) operator splitting (treating each equation independently), the use of the average of the limitors for each equation, limiting based on some "key variable" (pressure, entropy), and others [74].

(b) Entropy is not always monotonic for FCT. This may be due to the low order scheme employed. It is obvious that the ultimate low order scheme is Godunov's scheme [75–78], but this scheme is much more expensive that the simple smoothers

currently in use [73,74]. A simpler, more efficient version of Godunov's scheme for unstructured grids should be developed.

(c) Steepeners for contact discontinuities: as contact discontinuities are linear, any scheme that does not possess a steepener will eventually flatten these out. Note that no physical argument leads to a distinction of linear and nonlinear discontinuities. Some kind of detection mechanism may be usefully incorporated for contact discontinuities.

6. SUPERCOMPUTER UTILIZATION

However good a method may be, if it does not lend itself to some form of parallelism, its future will always remain a dubious one. The speed–up ratio between a code that exploits the machine hardware and one that does not lies between 1:10 and 1:20 on today's vector machines. This performance ratio will go up drastically when massively parallel computing becomes available [79,80]. Fortunately, the bigger the problem to be solved, the easier it is to exploit some inherent parallelism of an algorithm.

6.1 VECTOR PROCESSING

On vector machines the important factors that determine the performance of an algorithm are DO–loop length and contiguity in memory (even on a CRAY!). Normally, the vector length in CFD codes for element subroutines is of order 8–10, far too short to exploit vector–machine hardware. The only way to achieve acceptable vector–lengths is to perform the assembly process on groups of elements, possibly the whole grid at once. This means that one–element type codes should be favored, in contrast to the more usual many–element type code now in use in industry.

Three different types of DO–loops are most often encountered:

(a) Loops over the same type of data: these are loops which involve only one type of data (either point or element data) and are the "favorites" of vector machines.

(b) GATHER–loops: this type of loop appears when point information needs to be processed at the element level (a point may be shared by several elements). Most vector machines have hardware–tailored GATHER devices, but this type of loop will, nevertheless, run between 2.5–5.0 times slower than type (a).

(c) SCATTER–ADD: these loops occur when assembling element contributions at points (e.g., formation of a right–hand side vector). As a point may receive contributions from several elements in the same loop, the simple SCATTER operation is not sufficient [81–83]. Coloring schemes have to be devised, and the original loop (over all the elements) has to be broken up into groups of elements so that the use of straight SCATTER operations becomes possible. This type of loop will run at roughly the same speed as the GATHER–loop.

6.2 PARALLEL PROCESSING

When speculating about parallel computing, one ought to distinguish between mildly parallel machines (up to 10 processors) and massively parallel machines. Examples of mildly parallel machines are the CRAY XMP/48 and the systems of array processors attached to a host machine. From a user's point of view, the main difficulties facing the development of codes on such a system are the poor FORTRAN capabilities and the very small local memory of the presently available array processors, as well as the very bad debugging software. Therefore, it pays off the rewrite only codes which have been thoroughly tested and will undergo no major modifications for these machines. In an area as dynamic as CFD, few codes ever made it to an array processor. However, FCT models have and with great success [84,85].

From a theoretical point of view, all algorithms which split the domain into sufficiently large subdomains are suited for mildly parallel machines. Examples of this kind are simple operator splitting (e.g., line by line, as long as the line is big enough), or the growing family of domain splitting algorithms [9,33].

6.3 REDUCTION OF MEMORY REQUIREMENTS

Schemes operating efficiently on unstructured grids require more memory than their structured grid counterparts. Among the possibilities that can be pursued in order to reduce memory requirements, we mention the following:

(a) Careful coding: an obvious possibility, but one that is usually considered only after a code has been shown to work (i.e., at a stage where as little as possible should be changed). Experience indicates that 30% reduction of memory may be achieved at the expense of 20% increase in CPU.

(b) Splitting into subdomains: the peak efficiency of vector machines is achieved for vector lengths that are only a fraction of the total number of grid points typically encountered when solving 3–D problems. The idea is then to save as much storage on temporal arrays as possible, performing all algorithmic steps (formation of right–hand sides, limiting, etc.) on subdomains. Memory requirements may be reduced by about 50% at the expense of some additional CPU time.

(c) Encasement of the unstructured grid in a structured grid: here, unstructuredness is only allowed close to the body where the highest geometrical/physical complexity is expected. At wider distances from the body, a structured grid is employed. This approach holds considerable promise of reducing requirements by more than an order of magnitude, but will require sophisticated programing and mesh generation capabilities.

7. SUPERCOMPUTER APPLICATIONS TO ROCKET COMBUSTION INSTABILITIES

7.1 GENERAL

The growth or decay of energy is responsible for instability or stability of waves in fluids, respectively. In general, there are three different sources of energy growth or decay.

They are: (1) pressure fluctuations (acoustic waves); (2) velocity fluctuations (hydrodynamic waves due to transition to turbulence, shear layers, or shedding of vortices);and (3) density fluctuations (intrinsic waves due to compressibility and/or chain reactions of unstable chemical radicals in combustion). Extensive research works have been carried out for acoustic instability [135–140] and hydrodynamic instability [140–143], with limited studies available on intrinsic instability [144]. Flandro [145] presented the energy balance method in which the acoustic energy equation was used to develop the nonlinear stability equation based on isentropic assumption and linear superposition of entropy change. Each of the above types of instability requires different methods of analyses and unification of such methods has not been attempted. The objective of the present paper is directed toward our desire to introduce a unified general method for wave instability analyses.

The basic approach toward this achievement, called the entropy controlled instability (ECI) method, is founded on the concept of entropy changes in which nonlinearity is a prime factor. This is because our ultimate goal is a general theory which enables nonlinear waves to be studied in detail without making simplified initial assumptions such as isentropy. Nonlinear waves invoke nonisentropy in which growth or decay of energy is properly accounted for. This line of thinking is dictated also by our desire to deal with compressible fluids, with a special case reduced to incompressible flows. To this end, we examine the energy equation written in terms of entropy changes as well as fluctuations of pressure, velocity, and density. Introducing spatial averages, or applying the Green–Gauss theorem, we integrate the energy equation by parts through which boundary surface integrals arise, playing the role of acoustic intensities. Additional terms representing the spatial growth of energy also arise in this process of integration by parts. Performing the time averages, we finally arrive at the nonlinear, nonisentropic stability equation, which assumes the form of nonlinear integro–ordinary differential equation for the energy growth factor indicative of stability or instability of waves. The integrands of

this nonlinear stability equation (the word 'nonisentropic' omitted but implied hereafter) are contributed from the results of the Navier–Stokes solutions using the Taylor–Galerkin finite elements [146–150]. The nonlinear stability equation will then be solved using the fourth order Runge–Kutta method to calculate the energy growth factor. It is shown that the general theory presented here is reduced to a simple linear theory of Cantrell and Hart [135] or Culick [136] as a special case with appropriate assumptions.

We shall discuss the details of these processes in the following sections.

7.2. ENTROPY CONTROLLED INSTABILITY (ECI) METHOD

7.2.1 NAVIER–STOKES SOLUTIONS

In order to perform stability analysis, it is necessary to first solve the unsteady Navier–Stokes equations representing the desired physics. To this end, the most general conservation form of Navier Stokes equations for compressible flows is written as

$$\frac{\partial \mathbf{U}}{\partial t} + \frac{\partial \mathbf{F}_j}{\partial x_j} + \frac{\partial \mathbf{G}_j}{\partial x_j} = \mathbf{B} \tag{1}$$

where

$$\mathbf{U} = \begin{bmatrix} \rho \\ \rho\, v_i \\ \rho\, E \\ \rho\, Y_k \end{bmatrix} \quad \mathbf{F}_j = \begin{bmatrix} \rho\, v_j \\ \rho\, v_i v_j + p\delta_{ij} \\ \rho\, E v_j + p v_j \\ \rho\, Y_k v_j \end{bmatrix} \tag{1a,b}$$

$$\mathbf{G}_j = \begin{bmatrix} 0 \\ -\tau_{ij} \\ -\tau_{ij} v_i + q_j \\ \rho\, D Y_{k,j} \end{bmatrix} \quad \mathbf{B} = \begin{bmatrix} 0 \\ \rho \sum_{k=1}^{N} Y_k f_{ki} \\ \rho \sum_{k=1}^{N} Y_k f_{ki} v_i \\ w_k \end{bmatrix} \tag{1c,d}$$

where τ_{ij} is the viscous stress tensor

$$\tau_{ij} = \mu \left(v_{i,j} + v_{j,i} - \frac{2}{3} v_{k,k} \delta_{ij} \right) \tag{1e}$$

and E is the stagnation energy

$$E = e + \frac{1}{2} v_i v_i = c_p T - \frac{p}{\rho} + \frac{1}{2} v_i v_i \tag{1f}$$

and f_{ki} is the body force and q_j is the heat flux vector.

$$q_j = -\lambda T_{,j} + \rho D \sum_{k=1}^{N} H_k Y_{k,j} \tag{1g}$$

Here, λ and D are the thermal conductivity and mass diffusivity, respectively. H_k is the total enthalpy of species k, Y_k is the mass fraction for the species k, and w_k is the reaction rate for the species k. Note that all derivatives are covariant in case of cylindrical coordinates.

For turbulent flows we add to (1) additional transport equations for turbulent kinetic energy and dissipation energy (k–ϵ model), respectively,

$$\frac{\partial}{\partial t}(\rho k) + \frac{\partial}{\partial x_j}\left(\rho v_j k - \mu_k \frac{\partial k}{\partial x_j}\right) = G - \rho\epsilon \tag{1h}$$

$$\frac{\partial}{\partial \rho}(\rho \epsilon) + \frac{\partial}{\partial x_j}\left(\rho v_j \epsilon - \mu_\epsilon \frac{\partial \epsilon}{\partial x_j}\right) = c_1 \frac{\epsilon}{k} G - c_2 \rho \epsilon^2 / k \tag{1i}$$

where G is the turbulent thermal dissipation energy transport and

$$\mu_k = \mu + \frac{\mu_t}{\sigma_k}, \qquad \mu_\epsilon = \mu + \frac{\mu_t}{\sigma_\epsilon}, \qquad \mu_t = \rho c_\mu \frac{k^2}{\epsilon},$$

$$c_\mu = 0.09, \qquad c_1 = 1.44, \qquad c_2 = 1.92, \qquad \sigma_k = 1.0, \qquad \sigma_\epsilon = 1.3$$

Appropriate modifications to the equations of momentum and energy and the suitable turbulent combustion model should be included as detailed in [146].

The solution procedure using the Taylor–Galerkin method are found in [147–151], which will not be repeated here. Examples include shock waves contributing to nonlinear, nonisentropic combustion instabilities for the space shuttle main engine combustion/thrust chamber and the side–burning solid propellant rocket motors. Calculations of energy growth factors and stability criteria are discussed below.

7.2.2 NONLINEAR, NONISENTROPIC STABILITY ANALYSIS

With the solutions of unsteady Navier–Stokes equations for the time–dependent periodic oscillatory initial boundary conditions available, we now turn to the entropy controlled instability (ECI) method of determining the unstable wave phenomena. To introduce entropy changes in the energy equation, we begin with thermodynamic relations for an ideal nonisentropic gas and write the pressure gradients in terms of density and entropy gradients,

$$p_{,i} = a^2 \rho_{,i} + \frac{\rho a^2}{c_p} S_{,i} \tag{2}$$

where a is the speed of sound, S is the specific entropy, and the comma denotes the partial derivative with respect to x_i. The gradient of the stagnation energy, E, assumes the form

$$E_{,i} = (c_p T - \frac{p}{\rho} + \frac{1}{2} v_j v_j)_{,i} \tag{3}$$

where the repeated indices imply summing. Performing the differentiation implied in (2) results in

$$E_{,i} = \frac{c_v}{R\rho} p_{,i} - \frac{c_v}{R} \frac{p}{\rho^2} \rho_{,i} + v_j v_{j,i} \tag{4}$$

where R is the specific gas constant. Substituting (2) into (4) yields

$$\rho E_{,i} = \frac{p}{\rho} \rho_{,i} + \frac{p}{R} S_{,i} + \rho v_j v_{j,i} \tag{5}$$

Let us now examine the conservation form of the energy equation

$$\frac{\partial}{\partial t} (\rho E) + (\rho E v_i - \sigma_{ij} v_j + q_{i,i})_{,i} = 0 \tag{6}$$

where σ_{ij} is the stress tensor

$$\sigma_{ij} = - p\delta_{ij} + \mu (v_{i,j} + v_{j,i} - \frac{2}{3} v_{k,k} \delta_{ij}) \tag{7}$$

Substituting (5) into (6) gives

$$\frac{\partial}{\partial t} (\rho E) + E(\rho v_i)_{,i} + v_i \left[\frac{p}{\rho} \rho_{,i} + \frac{p}{R} S_{,i} + \rho v_j v_{j,i}\right] - (\sigma_{ij} v_j)_{,i} + q_{i,i} = 0 \tag{8}$$

This is the entropy controlled energy equation, instrumental in determining the nonlinear wave instability.

The pressure, velocity, and density may be written in the form

$$p = \bar{p} + p' \tag{9a}$$

$$v_i = \bar{v}_i + v_i' \tag{9b}$$

$$\rho = \bar{\rho} + \rho' \tag{9c}$$

where the symbols, bar and prime, denote the mean and fluctuation parts, respectively. From thermodynamic relations we may write the entropy difference in the form

$$S - S_0 = R\ell n \left[\left(1 + \frac{p'}{\bar{p}}\right)^{\frac{1}{\gamma-1}} \left(1 + \frac{\rho'}{\bar{\rho}}\right)^{-\frac{\gamma}{\gamma-1}} \right] \tag{10}$$

Expanding the RHS of (10) in infinite series and after some algebra, we obtain

$$S = R \left[S_{(1)} + S_{(2)} + S_{(3)} + S_{(4)} + \ldots \right] + S_0 \tag{11}$$

where S_0 is the entropy at the initial state ($S_0 = 0$), and

$$S_{(1)} = \frac{1}{\gamma-1} \frac{p'}{\bar{p}} - \frac{\gamma}{\gamma-1} \frac{\rho'}{\bar{\rho}}$$

$$S_{(2)} = -\frac{1}{2} \left[\frac{1}{\gamma-1} \left(\frac{p'}{\bar{p}}\right)^2 - \frac{\gamma}{\gamma-1} \left(\frac{\rho'}{\bar{\rho}}\right)^2 \right]$$

$$S_{(3)} = \frac{1}{3} \left[\frac{1}{\gamma-1} \left(\frac{p'}{\bar{p}}\right)^3 - \frac{\gamma}{\gamma-1} \left(\frac{\rho'}{\bar{\rho}}\right)^3 \right]$$

$$S_{(4)} = -\frac{1}{4} \left[\frac{1}{\gamma-1} \left(\frac{p'}{\bar{p}}\right)^4 - \frac{\gamma}{\gamma-1} \left(\frac{\rho'}{\bar{\rho}}\right)^4 \right]$$

Here the terms with fifth order or higher are neglected, assuming that they are negligible.

To obtain acoustic energy equation, we apply the Green–Gauss theorem or integrate (8) by parts and take a time average in the form

$$\left\langle \int_\Omega \frac{\partial}{\partial t} (\rho E)\, d\Omega + \int_\Gamma \left[E\rho v_i n_i + v_i (p\, n_i + \frac{p}{R} S\, n_i + \rho\, v_j v_j\, n_i) - \sigma_{ij} v_j\, n_i - \lambda\,(T)\, T_{,i}\, n_i \right. \right.$$

$$+ \rho D \sum_{k=1}^{N} c_{pk} T Y_{k,i} n_i \Big] d\Gamma - \int_\Omega \Big[E_{,i} \rho v_i + \rho \left(v_i \frac{p}{\rho} \right)_{,i} + \left(v_i \frac{p}{R} \right)_{,i} S + \left(\rho v_i v_j \right)_{,i} v_j$$

$$+ \left(\lambda(T) \right)_{,i} T_{,i} - \left(\rho D \sum_{k=1}^{N} c_{pk} T \right)_{,i} Y_{k,i} \Big] d\Omega \rangle = 0 \qquad (12)$$

where Ω and Γ represent the domain and boundary surface, respectively, $\langle \cdot \rangle$ implies time averages and n_i denotes the component of a vector normal to the surface.

It is interesting to note that the domain integral terms (last four terms) arise as a result of the integration by parts implying the spatial growth of energy. This spatial growth of energy is in addition to the usual temporal growth of energy indicated by the domain integral with the time derivative (first term in (8)). Let ϵ be the energy growth factor, stable for $0 \leq \epsilon \leq 1$, unstable for $\epsilon > 1$, with $\epsilon=1$ indicating the neutral stability. The fluctuation terms in (9) and (11) contribute to (12) as multiples of higher order fluctuations. Multiplying the like powers of ϵ with the fluctuation terms of the same order and retaining the terms up to and including the fourth order, we obtain

$$\langle \int (\cdot)\, d\Omega \rangle = \langle \int_\Omega (\delta_0 + \epsilon\delta_1 + \epsilon^2\delta_2 + \epsilon^3\delta_3 + \epsilon^4\delta_4 + \ldots)\, d\Omega \rangle \qquad (13a)$$

$$\langle \int_\Gamma (\cdot)\, d\Gamma \rangle = \langle \int_\Gamma (\phi_0 + \epsilon\phi_1 + \epsilon^2\phi_2 + \epsilon^3\phi_3 + \epsilon^4\phi_4 + \ldots)\, d\Gamma \rangle \qquad (13b)$$

Here δ_0 and ϕ_0 contain only the mean quantity, δ_1, δ_2, δ_3, δ_4 and ϕ_1, ϕ_2, ϕ_3, ϕ_4 are referred to as the first, second, third, and fourth order perturbations capable of growth and decay in acoustic energy as dictated by the magnitudes of ϵ, growing if $\epsilon > 1$ and decaying if $\epsilon < 1$. Notice that the relations in (9a, b, and c) imply that the Navier–Stokes solutions are obtained with the initial condition $\epsilon = 1$ and the energy in (13) may grow or decay in accordance with the magnitude of ϵ from the initial or reference state $\epsilon = 1$.

Performing the differentiation as implied in (12), we obtain

$$\frac{\partial}{\partial t} (\epsilon^2 E_1 + \epsilon^3 E_2 + \epsilon^4 E_3) = \epsilon^2 I_1 + \epsilon^3 I_2 + \epsilon^4 I_3 \qquad (14)$$

in which the zeroth order terms are canceled and first order terms vanish due to time averages. Notice that the time averages are contained in $E_{(i)}$ and $I_{(i)}$. Here, the energy

growth factor ϵ is an explicit function of time. However, $E_{(i)}$ is no longer an explicit function of time because of its time averages. Thus the partial derivative with respect to time in (14) involves only ϵ, not $E_{(i)}$, so that

$$\frac{d\epsilon}{dt} = \frac{\epsilon^2 I_1 + \epsilon^3 I_2 + \epsilon^4 I_3}{2\epsilon E_1 + 3\epsilon^2 E_2 + 4\epsilon^3 E_3}$$

or

$$\frac{d\epsilon}{dt} = (\epsilon I_1 + \epsilon^2 I_2 + \epsilon^3 I_3)\frac{1}{2E_1}\left\{1 - \epsilon\frac{3E_2}{2E_1} + \epsilon^2\left[\frac{9}{4}\left(\frac{E_2}{E_1}\right) - \frac{2E_3}{E_1}\right]\right\} \tag{15}$$

where higher order terms and those terms much smaller than unity have been neglected.

It follows from (15) that the nonlinear stability equation takes the form

$$\frac{d\epsilon}{dt} - \alpha_1\epsilon - \alpha_2\epsilon^2 - \alpha_3\epsilon^3 = 0 \tag{16}$$

This is a form identical to Flandro [145], although the basic approach to the formulation and the solution procedures differ. Here α_1, α_2, and α_3 are energy growth rate parameters of first, second, and third order, respectively.

$$\alpha_1 = \frac{1}{2E_1} I_1 \tag{17a}$$

$$\alpha_2 = \frac{1}{2E_1}\left(I_2 - \frac{3E_2}{2E_1} I_1\right) \tag{17b}$$

$$\alpha_3 = \frac{1}{2E_1}\left\{I_3 - \frac{3E_2}{2E_1} I_2 + \left[\frac{9}{4}\left(\frac{E_2}{E_1}\right)^2 - \frac{2E_3}{E_1}\right] I_1\right\} \tag{17c}$$

with

$$E_1 = \left\langle \int_\Omega a^{(1)}\, d\Omega \right\rangle \tag{18a}$$

$$E_2 = \left\langle \int_\Omega a^{(2)}\, d\Omega \right\rangle \tag{18b}$$

$$E_3 = \left\langle \int_\Omega a^{(3)}\, d\Omega \right\rangle \tag{18c}$$

$$I_1 = \left\langle \int_\Omega b^{(1)}\, d\Omega \right\rangle - \left\langle \int_\Gamma c_i^{(1)}\, n_i\, d\Gamma \right\rangle \tag{19a}$$

$$I_2 = \langle \int_\Omega b^{(2)}\, d\Omega \rangle - \langle \int_\Gamma c_i^{(2)}\, n_i\, d\Gamma \rangle \tag{19b}$$

$$I_3 = \langle \int_\Omega b^{(3)}\, d\Omega \rangle - \langle \int_\Gamma c_i^{(3)}\, n_i\, d\Gamma \rangle \tag{19c}$$

Explicit forms of $a^{(1)}$, $b^{(1)}$, and $c^{(1)}$ will be discussed in Section 3 and the integrands for the second and third order growth parameters are shown in Appendix A. The physical significance and interpretations of the above process will be discussed in the following subsection.

7.2.3 PHYSICAL INTERPRETATION

The physical significance in the above development may be schematically demonstrated as shown in Fig. 1. First, unsteady Navier–Stokes solutions with time dependent oscillatory initial boundary conditions are obtained at each computational grid as shown in Fig. 1a. A typical variable vs time, (Fig. 1b), at any grid point (finite element node) may exhibit sawtooth type wave forms as well as sinusoidal waves. Imagine that several variables at each of the several thousand nodes present themselves in the form as shown in Fig. 1b. Each wave form of different frequencies at different spatial locations is expected to contribute to the overall stability or instability. Take one complete peak wave form period as indicated by $\tau = n\Delta t$ where Δt is the Navier–Stokes time step with n usually being in the range between teens and hundreds.

Performing the time average for this time period ($n\Delta t$), we obtain the mean quantity ($\bar{f}$) of the variable f. Then the disturbance (fluctuation) part f' is calculated as

$$f' = f - \bar{f}$$

where f is the Navier–Stokes solution.

From these data, spatial integrations involving both domain and boundary surfaces and time averages (Fig. 1a) as dictated by (18) and (19) are then carried out. Here, $\int_\Omega a^{(n)}\, d\Omega$ denotes the temporal growth of energy, whereas $\int_\Omega b^{(n)}\, d\Omega$ represents the spatial

growth of energy. The boundary integral $\int_\Gamma c_i^{(n)}\, n_i\, d\Gamma$ indicates the acoustic intensity. For combustion chamber applications, the burning surface admittance, response functions, or information on nozzle entrance or acoustic liner, etc., can be initially imposed on the Navier–Stokes solutions as boundary conditions to generate the oscillatory motions as depicted in Fig. 1b. These boundary data, however, reappear as called for in the integrand, $c_i^{(n)}$, in (19). They act as acoustic intensity and eventually contribute to the determination of stability or instability of the system.

The ingredients of $a^{(n)}$, $b^{(n)}$, and $c_i^{(n)}$ arise from fluctuation parts of the Navier–Stokes solutions as well as the mean parts. These fluctuations through the temporal growth of energy $a^{(n)}$, spatial growth of energy $b^{(n)}$, and acoustic intensity $c_i^{(n)}$, are responsible for driving the system toward instability. The consequences lead to determination of the energy growth factor vs time as shown in Fig. 1c by solving the nonlinear stability equation (16). It is important to realize that the Navier–Stokes solutions and the nonlinear stability equation (16) encompass acoustic waves, hydrodynamic (vortical or shear layer) waves, intrinsic (density fluctuations or chemically reacting combustion) waves, or combined effects of all types of wave interactions.

Notice that, in (6) and (12), heat flux changes are not directly involved. This is because the spatial integration of fluctuations of heat flux or temperature vanishes upon time averages. However, fluctuations of temperature and chemical species mass fractions have been included in the Navier–Stokes solutions of (1), thus indirectly contributing to the fluctuations of density (ρ') in the stability calculations.

Some comments on the mean pressure changes (DC shifts), pressure coupling, velocity coupling, limit cycles, and triggering are in order. These phenomena often observed in solid propellant combustion chambers, would appear in the flowfield under appropriate initial and boundary conditions during the Navier–Stokes calculations. The purpose of the ECI method is merely to determine whether the flowfield containing such

physical phenomena is stable or unstable. It is emphasized that all physical phenomena are expected to prevail and be identified in the solution of Navier–Stokes equations, which are then reconfirmed in the stability analysis.

7.3. LINEAR INSTABILITY

To gain an insight into the solution of (16), we may neglect the last two terms associated with the second and third order energy growth rate parameters and write

$$\frac{d\epsilon}{dt} - \alpha_1 \epsilon = 0 \tag{20}$$

which yields a solution in the form

$$\ln \epsilon = \alpha_1 t + c_1 \tag{21}$$

To establish an initial condition, we assume neutral stability $\epsilon = 1$ at $t = 0$. This gives $c_1 = 0$. Thus, the solution takes the form

$$\epsilon = e^{\alpha_1 t} \tag{22}$$

Under this initial condition, there exists a unique solution for any given α_1 with $t > 0$. The stability criteria are:

Stable: $0 \leq \epsilon \leq 1$ with $-\infty < \alpha_1 < 0$

Neutral stability: $\epsilon = 1$ with $\alpha_1 = 0$

Unstable: $1 < \epsilon \leq \infty$ with $0 < \alpha_1 < \infty$

Although these criteria are not applicable for the nonlinear equation (16) when α_2 and α_3 are involved, the same initial condition, $\epsilon_1 = 1$ at $t = 0$, as originally defined in (13a, b), can be used. That is, there exists a unique solution ϵ for any given α_1, α_2 and α_3 with $t > 0$. Therefore, the criteria for stability in terms of ϵ remain the same with various combinations of α_1, α_2, and α_3.

7.3.1 NONISENTRIPIC CASE

Notice that the integration involved in the growth rate parameters α_1, α_2, and α_3 and the subsequent solution of the nonlinear ordinary differential equation (16) are formidable. However, it would be informative to examine the case of linear instability ($\alpha_2 = 0$, $\alpha_3 = 0$) given by (20) but with nonisentropy. Therefore, the first order energy growth rate parameter takes the form, from (20) and (17a),

$$\alpha_1 = \frac{1}{\epsilon}\frac{d\epsilon}{dt} = \frac{I_1}{2E_1} = \frac{\langle \int_\Omega b^{(1)} d\Omega \rangle - \langle \int_\Omega c_i^{(1)} \, n_i d\Gamma \rangle}{\langle 2 \int a^{(1)} \, d\Omega \rangle} \tag{23}$$

Assuming that the fluid is inviscid ($\mu = 0$) the explicit forms of integrals in (23) become

$$\int_\Omega a^{(1)} \, d\Omega = \int_\Omega (\frac{\bar{\rho}}{2} v_j' v_j' + \rho' \bar{v}_j v_j') \, d\Omega \tag{24a}$$

$$\begin{aligned}
\int_\Omega b^{(1)} \, d\Omega = \int_\Omega \Big\{ & \bar{\rho}\bar{v}_i \Big(-\frac{p'\rho'}{(\gamma-1)\bar{\rho}^2} + \frac{\bar{p}\rho'^2}{(\gamma-1)\bar{\rho}^3} + \frac{1}{2} v_j' v_j'\Big)_{,i} + (\bar{\rho} v_i' + \bar{v}_i \rho')\Big(\frac{p'}{(\gamma-1)\bar{\rho}} \\
& - \frac{\bar{p}\,\rho'}{(\gamma-1)\bar{\rho}^2} + \bar{v}_j v_j'\Big)_{,i} + v_i'\rho'\Big(\frac{\bar{p}}{(\gamma-1)\bar{\rho}} + \frac{1}{2}\bar{v}_j\bar{v}_j\Big)_{,i} + \bar{\rho}\,\Big(-\frac{\bar{v}_i p'\rho'}{\bar{\rho}^2} + \frac{\bar{v}_i\bar{p}}{\bar{\rho}^3}\rho'^2 \\
& + \frac{p'v_i'}{\bar{\rho}} - \frac{\bar{p}v_i'\rho'}{\bar{\rho}^2}\Big)_{,i} + \rho'\Big(\frac{\bar{v}_i p'}{\bar{\rho}} - \frac{\bar{p}\bar{v}_i\rho'}{\bar{\rho}^2} + \frac{\bar{p}v_i'}{\bar{\rho}}\Big)_{,i} + \Big(\frac{p'}{(\gamma-1)\bar{p}} - \frac{\gamma\rho'}{(\gamma-1)\bar{\rho}}\Big)(\bar{p}v_i' \\
& + p'\bar{v}_i)_{,i} + \Big(-\frac{p'^2}{2(\gamma-1)\bar{p}^2} + \frac{\gamma\rho'^2}{2(\gamma-1)\bar{\rho}^2}\Big)(\bar{p}\bar{v}_i)_{,i} + \bar{v}_j\,(\bar{\rho}v_i'v_j' + \rho'\bar{v}_j v_i' \\
& + \rho'\bar{v}_i v_j')_{,i} + v_j'\,(\bar{\rho}\bar{v}_i v_j' + \bar{\rho}\,v_i'\bar{v}_j + \rho'\bar{v}_i\bar{v}_j)_{,i}
\end{aligned} \tag{24b}$$

$$\int_\Gamma c_i^{(1)} n_i d\Gamma = \int_\Gamma \Big\{ \bar{\rho}\bar{v}_i \Big(-\frac{p'\rho'}{(\gamma-1)\bar{\rho}^2} + \frac{\bar{p}\rho'^2}{(\gamma-1)\bar{\rho}^3} + \frac{1}{2} v_j' v_j'\Big) + (\bar{\rho}\, v_i' + \bar{v}_i \rho') \Big(\frac{p'}{(\gamma-1)\bar{\rho}}$$

$$- \frac{\bar{p}\rho'}{(\gamma-1)\bar{\rho}^2} + \bar{v}_j v_j'\Big) + \rho' v_i' \Big(\frac{\bar{p}}{(\gamma-1)\bar{\rho}} + \frac{1}{2}\bar{v}_j \bar{v}_j\Big) + p' v_i' + \Big(-\frac{p'^2}{2(\gamma-1)\bar{\rho}^2}$$

$$+ \frac{\gamma\rho'^2}{2(\gamma-1)\bar{\rho}^2}\Big)\bar{p}\bar{v}_i + \Big(\frac{p'}{(\gamma-1)\bar{p}} - \frac{\gamma\rho'}{(\gamma-1)\bar{\rho}}\Big)(\bar{p}v_i' + p'\bar{v}_i) + \bar{v}_i\,(\bar{\rho}v_j' v_j'$$

$$+ 2\rho'\bar{v}_j v_j') + v_i'\,(2\bar{\rho}\bar{v}_i v_i' + \rho'\bar{v}_i\bar{v}_i) + v_i'\,p'\Big\}\, n_i\, d\Gamma \qquad (24c)$$

Notice that the first term on RHS of (24a) represents the kinetic energy of the sound wave. If isentropic assumption is made, then ρ' can be expanded into infinite series in terms of p', p'^2, ... such that the second term on the RHS of (24a) contains the potential energy of the sound wave usually identified in the linear acoustic energy equation. However, our objective here is to allow entropy to change and, therefore, we must keep ρ' to remain subjected to nonisentropy. Another important observation is the domain integral for $b^{(1)}$ which has appeared for the first time as a result of the integration by parts (24b), signifying the spatial growth of energy. The boundary integral for $c_i^{(1)} n_i$ contains the terms of acoustic intensity normally identified in the linear acoustics, but significantly in a different form. Additional terms which arise in the process developed in this analysis will allow determination of stability or instability of wave motions with explicit changes of entropy contributing to the growth or decay of energy. However, it is not possible to evaluate the integrals (24a, b, c) because the density fluctuations ρ' cannot analytically be determined. This difficulty can be resolved in a certain special case if isentropy is assumed as discussed below.

7.3.2. ISENTROPIC CASE

If the flow is isentropic then it can be shown that

$$\rho' = \frac{p'}{\bar{a}^2} + \frac{1}{2}\bar{\rho}\frac{1-\gamma}{\gamma^2}\frac{p'^2}{\bar{p}^2} + \frac{1}{6}\frac{\bar{\rho}(1-\gamma)(1-2\gamma)}{\gamma^3}\frac{p'^3}{\bar{p}^3} + \frac{1}{24}\frac{\bar{\rho}(1-\gamma)(1-2\gamma)(1-3\gamma)}{\gamma^4}\frac{p'^4}{\bar{p}^4} + \ldots \qquad (25)$$

where $\bar{a}$ denotes the speed of sound without flow. As far as the linear stability is concerned only the first two terms on the RHS of (25) will contribute to (24a, b, c) as seen from substitution of (25) into (9c) and subsequently to (24a,b,c).

$$\int_\Omega a^{(1)}\,d\Omega = \int_\Omega \left(\frac{\bar{\rho}}{2}v_j'v_j' + \frac{p'^2}{2\bar{\rho}\bar{a}^2} + \frac{\bar{v}_j v_j' p'}{\bar{a}^2}\right) d\Omega \qquad (26a)$$

$$\int_\Omega b^{(1)}\,d\Omega = \int_\Omega \left\{\bar{\rho}\bar{v}_i\left(\frac{p'^2}{(\gamma-1)\bar{\rho}^2\bar{a}^2} + \frac{\bar{p}p'^2}{(\gamma-1)\bar{\rho}^3\bar{a}^4} + \frac{1}{2}v_j'v_j' + \ldots\right)_{,i} + \ldots\right\} d\Omega \qquad (26b)$$

$$\int_\Gamma c_i^{(1)} n_i\,d\Gamma = \int_\Gamma \left\{p'v_i' + \frac{p'^2\bar{v}_i}{\bar{\rho}\bar{a}^2} + \bar{\rho}\,v_i'\bar{v}_j v_j' + \frac{p'\bar{v}_i\bar{v}_j v_j'}{\bar{a}^2} + \ldots\right\} n_i\,d\Gamma \qquad (26c)$$

Since ρ' does not appear in the integrals of (26a, b, c) it is now possible to substitute analytical forms of p' and v_i' in terms of time dependent acoustic eigenfunctions and perform explicit analytical integrations. However, it is clear that the additional domain integral (26b) and many more additional terms arising as a result of the entropy controlled energy equation given by (8) or (12) will produce the results quite contrary to the traditional isentropic solution, (see Cantrell and Hart [135] or Culick [136]).

$$\alpha_1 = \frac{-\left\langle \int_\Gamma \left[p'v_i' + \frac{p'^2\bar{v}_i}{\bar{\rho}\bar{a}^2} + \bar{\rho}\,v_i'\bar{v}_j v_j' + \frac{p'\bar{v}_i\bar{v}_j v_j'}{\bar{a}^2}\right] n_i\,d\Gamma\right\rangle}{2\left\langle \int_\Omega \left(\frac{1}{2}\bar{\rho}\,v_j'v_j' + \frac{p'^2}{2\bar{\rho}\bar{a}^2} + \frac{\bar{v}_j v_j' p'}{\bar{a}^2}\right) d\Omega\right\rangle} \qquad (27)$$

Note that the terms on the numerator are the same as the first four terms of (26c) with the negative sign as indicated in (19a), and the terms of the denominator are identical to those in (26a). However, the domain integral of (26b) is absent. This integral contributed by $b^{(1)}$ represents the spatial growth or decay of energy as balanced by the boundary conditions and acoustic intensities on the boundary surface. This is in contrast to the

temporal growth or decay of energy originating from (26a).

Despite the special feature in the proposed formulation, however, the analytical forms for p' and v_i' as used by Cantrell and Hart [1], are incapable of simulating sawtooth type shock waves. For example consider the acoustic field of a cylinder with the radius R and length L,

$$p' = \Re e \left[\bar{p} \cos \frac{\ell \pi x}{L} J_m (\beta_{mn} \frac{r}{R}) \cos (m\theta) e^{i\omega t} \right] \tag{28a}$$

$$v_i' = \Re e \left[\frac{i \bar{p}}{\omega \bar{\rho}} \cos \frac{\ell \pi x}{L} J_m (\beta_{mn} \frac{r}{R}) \cos (m\theta) e^{i\omega t} \right] \tag{28b}$$

Here angular frequency, ω, is defined as

$$\omega = \bar{a} \left[(\frac{\ell \pi}{L})^2 + (\frac{\beta_{mn}}{R}) \right]^{\frac{1}{2}}$$

with ℓ, m, n, being the positive integers or zero, J_{mn} the Bessel function of order m, and β_{mn} the nth root of $J_{mn}'(\beta) = 0$. Retaining only those terms arising from the standard acoustic energy equations (without employing the entropy controlled energy equation), a simple solution can be obtained using (28a, b) to calculate the linear energy growth rate parameter α_i as demonstrated by Cantrell and Hart [135]. If the entire terms implied in (26a, b, c) are used, however, it is no longer possible to obtain analytical solutions.

7.4 NONLINEAR INSTABILITY

Nonlinear, nonisentropic waves occur in many industrial propulsion combustion systems. Shock waves may interact with turbulent vortical waves or shear layers of liquid jets in gas medium. Density fluctuations due to chemical reactions may also be combined. We have seen that analytical solutions of even the linear instability by ECI method presented in the previous section are intractable. First of all, the fluctuation variables p', v_i', and ρ' are to be numerically calculated by solving the Navier–Stokes equations. Then we must perform numerical integrations required to evaluate the energy growth rate

parameters α_1, α_2, and α_3. Subsequently, numerical solutions of the nonlinear ordinary differential equation must be carried out.

Numerical integrations as required by (18a, b, c) and (19a, b, c) can be performed most efficiently by Galerkin finite element techniques to calculate the energy growth rate parameters α_1, α_2, and α_3 according to (17a, b, c). Finally the nonlinear ordinally differential equation (16) is solved using the Newton–Raphson method to determine the energy growth factor ϵ. Thus, it is seen that the determination of stability $(0 < \epsilon < 1)$, instability $(\epsilon > 1)$, or neutral stability $(\epsilon = 1)$ is made available for each $n\Delta t$ period and we move on until desired time is reached as shown in Fig. 1c. It is interesting to see that, in this decision making process of stability or instability, "all" nodal points (thousands of nodes) with their nodal values of "all" variables have participated. Every wave peak, whether sinusoidal or sawtooth type, has been recognized. Shock waves interacting with turbulence, shear layers, or shedding of vortices, or effects of chemical reactions can be reflected in calculations of (17 a, b, c) and could have eventually contributed to the solution of (16) for determination of stability or instability.

Solutions to the nonlinear ordinary differential equation (16) may be obtained using the fourth–order Runge–Kutta method. Iterations will continue until convergence.

7.5 SOLUTION PROCEDURE

It is clear that the solution consists of three parts. First the Navier–Stokes equations are solved. Then the results of the Navier–Stokes solutions are used to calculate the energy growth rate parameters. Finally the energy growth factor is computed by solving the nonlinear, nonisentropic stability equation. Step–by–step solution procedures are described as follows:

(1) With appropriate boundary and initial conditions, solve the Navier–Stokes equations. Initially, the mean pressure, $\bar{p}$, and temperature, T, based on the ideal

gas law, are specified everywhere. At the inlet for liquid propellants, however, the oscillatory pressure is specified [$p = \bar{p} + d \sin \omega t$)], where d is the % disturbance and ω is the frequency. For the solid propellants, the burning surface gas normal velocity (v) is computed from the response function and propellant burning rate such that $v = \bar{v}(1 + d \sin \omega t)$.

(2) Calculate p, v_i, ρ, and T. Taylor–Galerkin finite element method with adaptive meshes is used in Navier–Stokes solutions.

(3) Advance time steps (Δt) of Navier–Stokes solutions to obtain wave oscillations to cover at least one wave period. Δt is determined continuously which satisfies an acceptable Courant number.

(4) Take time averages for the period $n\Delta t$ with n chosen such that at least one peak wave period is covered. These time averages lead to $\bar{p}$, $\bar{v}_i$, and $\bar{\rho}$.

(5) Calculate the fluctuation quantities as $p' = p - \bar{p}$, $v_i' = v_i - \bar{v}_i$, $\rho' = \rho - \bar{\rho}$, where p, v_i, and ρ represent Navier–Stokes solutions.

(6) Calculate the energy growth rate parameters α_1, α_2, and α_3 from (17a, b, c) using the results of step 5, above.

(7) Solve the nonlinear differential equation (16) using the Runge–Kutta method with the initial condition $\epsilon = 1$ at $t = 0$, corresponding to neutral stability.

(8) Repeat steps 1 through 7 until the desired length of time has been advanced.

Note that for each time–average period in step 4, above, instability and stability are determined by $\epsilon > 1$ and $\epsilon < 1$, respectively, with $\epsilon = 1$ being the neutral stability. If the system is found to be unstable, it is not necessary to proceed to the next time step. However, for the entire ranges of time for which Navier–Stokes solutions are available, the stability analysis may be performed, even if instability has been found in previous time

steps. This is so because Navier–Stokes solutions are independent of the stability analysis as formulated here. Rather, the stability analysis here determines the state of stability or instability based on current flowfield as calculated from the Navier–Stokes solution. The following applications are based on computer code ECI–2.

7.6. APPLICATIONS

7.6.1 LIQUID PROPELLANTS

Case 1 Laminar Compressible Nonreacting Flows

Figure 2a shows the axisymmetric geometry of combustion/thrust chamber with 965 triangular elements and 528 nodes as a consequence of adaptive mesh process. Notice that in the vicinity of the walls approximately 80% of the nodes are concentrated resulting in prominent boundary layers. To demonstrate the capability of the code, initially, the steady state flow field without disturbances is examined. The velocity vectors and contours of Mach number, pressure, and temperature are shown in Fig. 2b, c, d, and e, respectively. Formation of boundary layers (Fig. 2b), separation of boundary layers and weak shock waves downstream (Fig. 2c, d), and decrease of temperature downstream and toward the wall (Fig. 2e) are evident.

With disturbances of d = 10%, 20% and 30% imposed on the mean pressures at the inlet, the Navier–Stokes transient analyses are performed. The time steps are continuously adjusted to satisfy acceptable Courant numbers, $0.2 \leq CN \leq 0.4$, for convergence. The graphical representation of oscillations of all variables at every node versus time is overwhelmingly complex. Therefore, wave forms only for d = 30% and $\bar{p}$ = 3000 psi at three selected positions, A at (1.8, 11.43 cm), B at (31.75, 11.43 cm), and C at (63.5, 6.55 cm) are shown in Fig. 3. Note that, although the sinusoidal input is provided at the inlet, the oscillations downstream become nonlinear, possibly of sawtooth type.

In Fig. 4, the energy growth factors ϵ for $\bar{p}$ = 500 psi are shown for various % disturbances. It is seen that for d = 10%, the energy growth factor remains in the stable region $\epsilon < 1$. The dotted lines and solid lines indicate the results for the linear (Eq. 20) and nonlinear (16) cases, respectively. As the disturbance increases (d = 20%) the energy growth factor reaches the neutral stability, $\epsilon = 1$ at $t \simeq 0.015$ sec. For d = 30%, the energy growth factor increases further ($\epsilon = 1.038$) at $t \simeq 0.2$ sec. Notice that the linear analysis underestimates the stability if stable whereas it underestimates the instability if unstable. The general trend is that instability is proportional to the percent disturbances.

As the mean pressure increases ($\bar{p}$ = 3000 psi), the possibility of instability increases as shown in Fig. 5, with the conclusion that instability is proportional to the mean pressure. Recall that for d = 10%, $\bar{p}$ = 500 psi, stability prevailed throughout whereas with d = 10%, $\bar{p}$ = 3000 psi neutral stability has been reached. The peak values of ϵ for $\bar{p}$ = 3000 psi are significantly larger than those for $\bar{p}$ = 500 psi.

Case 2 Turbulent Compressible Nonreacting Flows

The discretized geometry for a steady state turbulent compressible nonreacting flow is shown in Fig. 6a with a total of 2688 elements and 1416 nodes. As seen in Fig. 6b (velocity vectors) and Fig. 6c (Mach number contours), the boundary layers are thinner than in the case of laminar flow, leading to turbulent shock wave interactions. It is clear that gradients of pressure (Fig. 6d) and temperature (Fig. 6e) are larger than in the case of laminar flow.

Wave forms of transient turbulent nonreacting flow with disturbances, d = 30%, $\bar{p}$ = 3000 psi, at the three positions are shown in Fig. 7. Although the wave forms in turbulence at these positions do not seem much different from the case of laminar flow, it is quite possible that wave forms at other locations where turbulent velocity gradients are significant would be drastically changed in contrast to the laminar flow.

The energy growth factors for turbulent flow are shown in Fig. 8 for $\bar{p}$ = 500 psi and Fig. 9 for $\bar{p}$ = 3000 psi. It is interesting to see that the effect of turbulence is to increase instability as compared with the laminar flow. The general trend other than the turbulent effect, however, remains the same as the laminar flow. That is, instability is proportional to disturbances and the mean pressure. The linear analysis again shows that stability is underestimated if stable and instability is underestimated if unstable.

Case 3 Chemically Reacting Laminar Compressible Flows with Hydrogen/Oxygen Combustion

Figure 10 shows the discretized geometry for a steady state chemically reacting flow without disturbances. A total of 1580 elements and 844 nodes are used. The chemical reactions considered are shown in Appendix B. The mass fractions at the inlet are 0.111 for H_2 and 0.889 for O_2, and the inlet velocity is 500 m/s. In this analysis the effect of viscosity is ignored to ensure an enhanced computational convergence, which leads to a flow without boundary layers along the wall. Due to the finite rate chemistry and stiffness arising from the chemical source terms, the computational convergence is rather slow. In the region of chemical reactions the velocity is decreased (Fig. 10b) and the Mach number contours are spaced widely apart (Fig. 10c), resulting in a rapid increase of pressure (Fig. 10d), but no evidence of shock discontinuities (Fig. 10c, d) between the throat and the downstream nozzle area. Temperature increases in the region of combustion in a sharp contrast to the nonreacting cases (Fig. 2e and Fig. 6e).

The contours of 8 species are shown in Fig. 11, beginning with the reactants, hydrogen (Fig. 11a) and oxygen (Fig. 11b), followed by products, H (Fig. 11c), HO_2 (Fig. 11d), H_2O (Fig. 11e), H_2O_2 (Fig. 11f), O (Fig. 11g), and OH (Fig. 11h). It is observed that H_2 is depleted halfway between the inlet and throat whereas O_2 prevails further downstream before it is depleted behind the throat. Most of the products (including the radicals), H, HO_2, O, and OH rapidly increase from the inlet and become maximum as

they pass through the throat. In contrast, H_2O and H_2O_2 gradually increase downstream with a constant rate.

Figure 12 shows the wave forms of the transient chemically reacting flow with disturbances, d = 30% and $\bar{p}$ = 500 psi, at the three positions considered earlier. Notice that, with chemical reactions, the frequencies of waves are very low and the response is quite slow particularly at downstream locations. Once again, the results plotted in Fig. 12 are misleading because oscillations in other locations (over 800 nodes) may prove to be significantly different. After all, combustion instability is determined by the stability equation, not by the appearance of oscillations observed at random locations.

In Fig. 13, the energy growth factors for the chemically reacting flow are examined. First of all, the linear analysis (dotted line) shows an apparent faulty prediction of instability for d = 10%, in which the nonlinear analysis indicates $\epsilon \simeq 0$ throughout the time segment investigated. Obviously, this is an indication of unreliability of the linear analysis. For d = 20%, however, the linear analysis appears to give the consistent results similar to the earlier examples in that the linear analysis underestimates the stability when stable and underestimates the instability when unstable. The nonlinear analysis shows that, for d = 20% and d = 30%, the peak values of energy growth factors are significantly larger than the nonreacting cases. Does this imply that chemically reacting flows always tend toward instability? An affirmative answer to this question is premature. In fact the entire investigation presented here is subject to the future verification by experimental measurements.

7.6.2 SOLID PROPELLANTS

As an example we select the motor data used at Naval Weapons Laboratory (NWC, Motor #9 in [152]). The following propellant and gas data are used: propellant density ρ_s = 1689 kg/m^3; propellant burning rate v_0 = 0.24 in/s; response function R = 0.85 (frequency ω = 300 Hz) as determined from the NWC test data (see Fig. 14); burning

surface pressure $\bar{p}$ = 1000 psi; gas density ρ = 7.1 kg/m^3; burning surface normal velocity v = 0.784 m/s; gas temperature T = 2883°R; Reynolds number Re = 10,000; viscosity μ = 1.4138 x 10^{-5} kg/m/s.

For calculations required for the stability analysis, we use a smaller motor (L/D = 6) in order to reduce computer time with the geometry as shown in Fig. 15. The finite element intermediate and final adaptive meshes are shown in Fig. 16a and Fig. 16b, respectively. Pressure and velocity data at the burning surface are shown in Fig. 17a and Fig. 17b, respectively.

Fig. 18 shows the streamline contours $0.0 \leq \psi \leq 980$ with $\Delta\psi = 2.8$ as they reach the steady state condition. Here the Navier–Stokes time step is chosen to satisfy the Courant number equal to approximately 0.4. Steep velocity gradients are apparent in the vicinity of the nozzle.

Figs. 19 through 26 indicate wave motions at locations A and B (Fig. 15) for pressure, longitudinal velocity, and radial velocity. Note that, as disturbances increase from 10% to 80% at A, the frequency and amplitude for the pressure increase significantly as seen in Figs. 19a through 19d. The longitudinal velocity turns to steep–fronted N–waves as disturbances increase (Figs. 20c through 20d). Similar trends occur in the radial velocity as shown in Figs. 22a through 22d. At location B, the pressure peak is smaller than at A (Figs. 22a through 22d). The longitudinal velocity increases drastically and there is a clear evidence of shock waves as demonstrated by the steep–fronted wave forms as disturbances increase (Figs. 23a through 23d). The radial velocity, however, decreases significantly with waveforms being quite irregular particularly at large disturbances (Figs. 24a through 24d).

Figures 25 and 26 represent waterfall plots for pressure and longitudinal velocity modes, extended to time t = 0.12 sec. Initial pressure disturbances upon ignition disappear as time progresses, but as disturbances increase, wave motions become prominent at time

t = 0.05 sec. with the frequency of approximately 990 Hz (d = 50%, 80%) as shown in Figs. 25a through d. For the longitudinal velocity (Figs. 26a through d), however, a prominent peaks occur at d = 30% at approximately 980 Hz but are gradually reduced as disturbances increase to 80%, but instead smaller peaks appear at 1300 Hz, 2500 Hz, 2500 Hz, and 3100 Hz. These phenomena correspond to the stability calculations as discussed below.

Finally, the energy growth factors for various % disturbances are shown in Figs. 27a through 27d. Solid and dotted lines represent the nonlinear (Eq. (16)) and linear (Eq. (20)) analyses, respectively. It is seen that stability condition ($0 \leq \epsilon \leq 1$) is maintained for $20\% \leq d \leq 50\%$ but instability ($\epsilon > 1$) occurs at t = 0.03 sec. for d = 80%. This corresponds to the waterfall peak at 990 Hz which begins at t = 0.03 sec. Recall, however, that the energy growth factor which determines instability represents the entire system behavior contributed from oscillations of all variables. It is interesting to note that the linear analysis always underestimates the stability if stable but underestimates the instability if unstable. It should be remarked that, for this short motor (L/D = 6), it took the large % disturbance (d = 80%) to cause the motor unstable. In a separate analysis with the full length motor (NWC #9 motor, L/D = 35.6) the motor became unstable at d = 20%.

7.7 CONCLUSIONS

The entropy controlled instability method has been applied to various problems in laminar flows, turbulent flows, and reacting flows for determination of stability conditions. The following conclusions are reached:

(1) Instability increases with an increase of disturbances.

(2) Instability increases with an increase of the mean pressure.

(3) Instability increases as laminar flows are changed to turbulent flows.

(4) Instability due to production of radicals under the finite rate chemistry is significant for the case investigated.

(5) The linear stability analysis underestimates stability if stable and underestimates instability if unstable.

(6) The correct stability analysis calls for at least the third order nonlinearity.

(7) Navier–Stokes solutions are capable of simulating the previously observed physical phenomena such as pressure and velocity coupling, flow turning, DC shifts, distributed combustion, pulsing, limit cycles, triggering, etc.

(8) Effects of all physical phenomena are then reflected in the energy growth rate parameters α_1, α_2, and α_3 and subsequently in the energy growth factor ϵ.

(9) Future studies are required to validate the present theory in comparison with experimental results for those cases other than examined in this paper.

8. CONCLUDING REMARKS

Unstructured grids, adaptive methods, and vector processing have been applied in developing a major computer code for the solution of reacting flow Navier–Stokes system and determination of combustion instabilities. Implementation of parallel processing is in progress and preliminary results are expected shortly.

This report does not include evaluation of codes developed by other organizations. Instead, the basic criteria for accuracy and efficiency have been established, and some applications have been made on rocket combustion problems. Research toward an ultimate goal, the most accurate and efficient CFD code, is in progress and will continue for years to come.

REFERENCES

1. Turkel, E., "Progress in Computational Physics", Comp. Fluids 11, 2, 121–144 (1983).

2. Jameson, A., "The Evolution of Computational Methods in Aerodynamics", ASME J. Appl. Mech. 50, 1052–1069, (1983).

3. Beam, R.M., and Warming, R.F., "An Implicit Finite Difference Algorithm for Hyperbolic Systems in Conservation–Law Form", J. Comp. Phys. 22, 87–220 (1978).

4. Mulder, W. "Multigrid Relaxation for the Euler Equations", J. Comp. Phys. 60, 235–252 (1985).
5. MacCormack, R.W., "A Numerical Method for Solving the Equations of Compressible Viscous Flow", AIAA J. 20, 1275–1281 (1982).

6. Patnaik, G., Boris, J.P., Guirguis, R.H., and Oran, E., "A Barely Implicit Correction for Flux–Corrected Transport", submitted to J. Comp. Phys. (1986).

7. Chung, T.J., **Finite Element Analysis in Fluid Dynamics**, McGraw–Hill, 1978.

8. Roach, P.J., **Computational Fluid Dynamics**, Hermosa, Albuquerque, NM, 1976.

9. Glowinski, R., Dinh, Q.V., and Periaux, J., "Domain Decomposition Methods for Nonlinear Problems in Fluid Dynamics", Comp. Meth. App. Mech. Eng. 40, 27–109 (1983).

10. Babuska, I., Chandra, J., and Flaherty, J.E., (eds), **Adaptive Computational Methods for Partial Differential Equations**, SIAM Philadelphia (1983).

11. Babuska, I., et al. (eds), **Accuracy Estimates and Adaptive Refinements in Finite Element Computations**, J. Wiley & Sons (1986).

12. Holst, T.L., Kaynak, U., Gundy, K.L., Thomas, S.D., and Flores, J., "Numerical Solution of Transonic Wing Flows Using an Euler/Navier–Stokes Zonal Approach", AIAA–85–1640 (1985).

13. Benek, J.A., Buning, P.G., and Steger, J.L., "A 3–D Chimera Grid Embedding Technique", AIAA–CP–85–1523 (1985).

14. Rai, M.M., "A Conservative Treatment of Zonal Boundaries for the Euler Equations", J. Comp. Phys. 62, 472–503 (1986).
15. Bristeau, M.O., Pironneau, O., Glowinski, R., Periaux, J., Perrier, P., and Poirier, G., "Application of Optimal Control and Finite Element Methods to the Calculation of Transonic Flows and Incompressible Viscous Flows". pp. 203–312 in **Proc. IMA Conf. on Num. Meth. in Appl. Fluid Mech.** (B. Hunt, ed), Academic Press (1980).

16. Jameson, A., Baker, T.J., and Weatherhill, N.P., "Calculation of Inviscid Transonic Flow over a Complete Aircraft", AIAA–86–0103 (1986).

17. Gnoffo, P.A., "A Finite–Volume, Adaptive Grid Algorithm Applied to Planetary Entry Flowfields", AIAA J. 21, 1249–1254 (1983)

18. Diaz, A.R., Kikuchi, N., and Taylor, J.E., "A Method for Grid Optimization for the Finite Element Method", Comp. Meth. Appl. Mech. Eng. 41, 29–45 (1983)

19. Nakahashi, K., and Deiwert, G.S., "A Three–Dimensional Adaptive Grid Method", AIAA–85–0486 (1985).

20. Palmerio, B., and Dervieux, A., "Application of a FEM Moving Node Adaptive Method to Accurate Shock Capturing", **Proc. 1st Int. Conference on Numerical Grid Generation in CFD**, Landshut, West Germany, July 14–17, Pineridge Press, 1986.

21. Shönauer, W., Raith, K., and Glotz, K., "The Principle of Difference Quotients as a Key to the Self–Adaptive Solution of Nonlinear Partial Differential Equations", Comp. Meth. Appl. Mech. Eng. 28, 327–359 (1981).

22. Dannenhoffer, J.F., and Baron, J.R., "Adaptive Procedure for Steady State Solution of Hyperbolic Equations", AIAA–84–0005 (1984).

23. Dannenhoffer, J.F., and Baron, J.R., "Grid Adaptation for the 2–D Euler Equations", AIAA–85–0484 (1985).

24. Dannenhoffer, J.F., and Baron, J.R., "Robust Grid Adaptation for Complex Transonic Flows", AIAA–86–0495 (1986).

25. Löhner, R., Morgan, K., and Zienkiewicz, O.C., "An Adaptive Finite Element Procedure for High Speed Flows", Comp. Meth. Appl. Mech. Eng. 51, 441–465 (1985).

26. Löhner, R., Morgan, K., and Zienkiewicz, O.C., "Adaptive Grid Refinement for the Compressible Euler Equations", Chapter 15 in **Accuracy Estimates and Adaptive Refinements in Finite Element Computations**, (I. Babuska et al, eds), J. Wiley & Sons (1980).

27. Palmerio, B., Billey, V., Dervieux, A., and Periaux, J., "Self–Adaptive Mesh Refinements and Finite Element Methods for Solving the Euler Equations", **Proc. ICFD Conference on Numerical Methods for Fluid Dynamics**, Reading, UK, March 1985.

28. Angrand, F., Billey, V., Dervieux, A., Periaux, J., Pouletty, C., and Stoufflet, B., "2–D and 3–D Euler Flow Calculations with a Second–Order Accurate Galerkin Finite Element Method", AIAA–85–1706 (1985).

29. Holmes, D.G., and Lamson, S.C., "Compressible Flow Solutions on Adaptive Triangular Meshes", Open Forum AIAA – Reno, 1986 – Meeting (1986).

30. Zienkiewicz, O.C., de S.R. Gago, J.P., and Kelly, D.W., "The Hierarchical Concept in Finite Element Analysis", Comp. Struct. 16, 53–65 (1983).

31. Löhner, R., and Morgan, K., "Improved Adaptive Refinement Strategies for Finite Element Aerodynamic Computations", AIAA–86–499 (1986).

32. Peraire, J., Vahdati, M., Morgan, K., and Zienkiewicz, O.C., "Adaptive Remeshing for Compressible Flow Computations", submitted to J. Comp. Phys. (1986).

33. Löhner, R., Morgan, K., and Zienkiewicz, O.C., "The Use of Domain Splitting with an Explicit Hyperbolic Solver", Comp. Meth. Appl. Mech. Eng. 45, 313–329 (1984).

34. Zienkiewicz, O.C., and Phillips, D.V., "An Automatic Mesh Generation Scheme for Plane and Curved Surfaces by Isoparametric Co–ordinates", Int. J. Num. Meth. Eng. 3, 519–528 (1971).

35. Ecer, A., Spyropoulos, J., and Maul, J.D., "A Three–Dimensional, Block–Structured Finite Element Grid Generation Scheme", AIAA J. 23, 10, 1483–1490, (1985).

36. Bowyer, A., "Computing Dirichlet Tesselations", The Computer J. 24, 2, 162–167 (1981).

37. Watson, D.F., "Computing the N–Dimensional Delaunay Tesselation with Application to Voronoi Polytopes", The Computer J. 24, 2, 167–172 (1981).

38. Tanemura, M., Ogawa, T., and Ogita, N., "A New Algorithm for Three–Dimensional Voronoi Tesselation", J. Comp. Phys. 51, 191–207 (1983).

39. Kirkpatrick, R.C., "Nearest Neighbor Algorithm", pp. 302–309 in **Springer Lecture Notes in Physics 238** (M.J. Fritts, W.P. Crowley and H. Trease eds), Springer–Verlag (1985)

40. Shenton, D.N., and Cendes, Z.J., "Three–Dimensional Finite Element Mesh Generation Using Delaunay Tesselation", IEEE Trans. on Magnetics, MAG–21, 2535–2538 (1985).

41. Coulomb, J.L., du Terrail, Y., and Meunier, G., "FLUX3D, a Finite Element Package for Magnetic Computation", IEEE Trans. on Magnetics, MAG–21, 2499–2502, (1985).

42. Yerry, M.A., and Shepard, M.S., "Automatic Three–Dimensional Mesh Generation by the Modified–Octree Technique", Int. J. Num. Meth. Eng. 20, 1965–1990 (1984).

43. Lo, S.H., "A New Mesh Generation Scheme for Arbitrary Planar Domains", Int. J. Num. Meth. Eng. 21, 1403–1426 (1985)

44. van Phai, N., "Automatic Mesh Generation with Tetrahedron Elements", Int. J. Num. Meth. Eng. 18, 237–289 (1982).

45. Thacker, W.C., Gonzalez, A., and Putland, G.E., "A Method for Automating the Construction of Irregular Computational Grids for Storm Surge Forecast Models", J. Comp. Phys. 37, 371–387 (1980).

46. Löhner, R., and Morgan, K., "Unstructured Multigrid Methods: First Experiences", **Proc. of the 3rd Int. Conference on Numerical Methods in Thermal Problems,** (R.W. Lewis, et al, eds), Pineridge Press, Swansea (1985).

47. Boris, J.P., "A Vectorized 'Nearest Neighbors' Algorithm of Order N Using a Monotonic Logical Grid", J. Comp. Phys. 66, 1–20 (1986).

48. Lambrakos, S.G., and Boris, J.P., "Geometric Properties of the Monotonic Logical Grid Algorithm for Near Neighbor Calculations", to appear in J. Comp. Phys. (1986).

49. Löhner, R., and Morgan, K., "An Unstructured Multigrid Method for Elliptic Problems", **Proc. of the 2nd European Multigrid Conference**, Köln, West Germany, October 1985.

50. Brand, K., **Multigrid Bibliography**, 3rd Edition, GMD, Bonn, West Germany (1983).

51. Hackbusch, W., and Trottenberg, U., (eds), **Multigrid Methods, Lecture Notes in Mathematics 960**, Springer–Verlag (1982).

52. Löhner, R., and Morgan, K., "An Unstructured Multigrid Method for Elliptic Problems", to appear in Int. J. Num. Meth. Eng. (1987).

53. Börgers, C., and Peskin, C.S., "A Lagrangian Method Based on the Voronoi Diagram for the Incompressible Navier–Stokes Equations on a Periodic Domain, pp. 87–113 in **Springer Lecture Notes in Physics 238** (M.J. Fritts, W.P. Crowley and H. Trease, eds), Springer–Verlag, (1985).

54. Hughes, T.J.R., Levit, M., and Winget, J., "Element–by–Element Implicit Algorithms for Heat Conduction", J. of Eng. Mech. 109, 2 (1983).

55. Hughes, T.J.R., Levit, M., and Winget, J., "An Element–by–Element Solution Algorithm for Problems in Structural and Solid Mechanics", Comp. Meth. Appl. Mech. Eng. 36, 241–254 (1983).

56. Ni, R.H., "A Multiple–Grid Scheme for Solving the Euler Equations", AIAA J. 20, 1565–1571 (1982).

57. Johnson, G.M., "Multiple–Grid Acceleration of Lax–Wendroff Schemes", NASA TM–82843 (1982).

58. Usab, W.J., and Murman, E.M., "Embedded Mesh Solutions of the Euler Equations Using a Multiple–Grid Method", pp. 447–472 in **Advances in Computational Transonics** (W.G. Habashi, ed), Pineridge Press, Swansea (1985).

59. Löhner, R., Morgan, K., and Kong, L., "An Unstructured Multigrid Method for the Compressible Euler Equations", **Proc of the 6th GAMM–Conference on Num. Meth. in Fluid Mech.** (D. Rues, W. Kordulla, eds), Vieweg Notes on Numerical Fluid Mechanics, Vol. 10, Vieweg Verlag (1986).

60. Jameson, A., Schmidt, W., and Turkel, E., "Numerical Solution of the Euler Equations by Finite Volume Methods Using Runge–Kutta Time–Stepping Schemes", AIAA Paper 81–1259 (1981).

61. Perez, E., "Finite Element and Multigrid Solution of the Two–Dimensional Euler Equations on a Non–Structured Mesh", INRIA Rep. 442 (1985).

62. Perez, E., Periaux, J., Rosenblum, J.P., Stoufflet, B., Dervieux, A., and Lallemand, M.H., "Adaptive Full–Multigrid Finite Element Methods for Solving the Two–Dimensional Euler Equations", **Proc. 10th Int. Conf. Num. Meth. Fluid Dynamics**, Peking, June 1986, Springer–Verlag (to appear).

63. Mavriplis, D., and Jameson, A., "Multigrid Solution of the Two–Dimensional Euler Equations on Unstructured Triangular Meshes", paper presented at the 1st World Congress of Computational Mechanics, Austin, TX, Sep. 22–26, (1986).

64. Oden, J.T., Devloo, P., and Strouboulis, T., "Adaptive Finite Element Methods for the Analysis of Inviscid Compressible Flow: I. Fast Refinement/Unrefinement and Moving Mesh Methods for Unstructured Meshes:, preprint (1986).

65. Löhner, R., "An Adaptive Finite Element Scheme for Transient Problems in CFD", submitted to Comp. Meth. Appl. Mech. Eng. (1986).

66. Fritts, M.J., Crowley, W.P., and Trease, H. (eds), **The Free–Lagrange Method, Springer Lecture Notes in Physics 238**, Springer–Verlag (1985).

67. Hughes, T.J.R., and Mallet, M., "A New Finite Element Formulation for Computational Fluid Dynamics: IV: A Discontinuity Capturing Operator for Multi–Dimensional Advective–Diffusive Systems", to appear in Comp. Meth. Appl. Mech. Eng. (1986).

68. Boris, J.P. and Book, D.L., "Flux–Corrected Transport. I. SHASTA, a Transport Algorithm that Works", J. Comp. Phys. 11, 38, (1973)

69. Book, D.L., Boris, J.P., and Hain, K., "Flux–Corrected Transport. II. Generalizations of the Method", J. Comp. Phys. 18, 248, (1975).

70. Boris, J.P., and Book, D.L., "Flux–corrected Transport. III. Minimal–Error FCT Algorithms", J. Comp. Phys. 20, 397–431 (1976).

71. Zalesak, S.T., "Fully Multi–Dimensional Flux–Corrected Transport Algorithm for Fluids", J. Comp. Phys. 31, 335–362 (1979).

72. Parrott, A.K., and Christie, M.A., "FCT Applied to the 2–D Finite Element Solution of Tracer Transport by Single Phase Flow in a Porous Medium", **Proc. of the ICFD Conf. on Numerical Methods in Fluid Dynamics**, Reading, Academic Press, 1986.

73. Löhner, R., Morgan, K., Vahdati, M., Boris, J.P., and Book, D.L., "FEM–FCT: Combining High Resolution with Unstructured Grids", submitted to J. Comp. Phys. (1986).

74. Löhner, R., Morgan, K., Vahdati, M., and Peraire, J., "Further Generalizations of FCT", in preparation (1986).

75. van Leer, B., "Towards the Ultimate Conservative Scheme. II. Monotonicity and Conservation Combined in a Second Order Scheme", J. Comp. Phys. 14, 361–370 (1974).

76. Roe, P.L., "Approximate Riemann Solvers, Parameter Vectors and Difference Schemes", J. Comp. Phys. 43, 357–372 (1981).

77. Osher, S., and Solomon, F., "Upwind Difference Schemes for Hyperbolic Systems of Conservation Laws", Math. Comp. 38, 339–374 (1982).

78. Colella, P., "Multi–dimensional Upwind Methods for Hyperbolic Conservation Laws", LBL–17023, Preprint, (1983).

79. Hockney, R.W., and Jesshope, C.R., **Parallel Computers**, Adam and Hilger (1981).

80. Schönaauer, W., and Gentzsch, W. (eds), "The Efficient Use of Vector Computers with Emphasis on CFD", Vieweg Notes on Numerical Fluid Mechanics, Vol. 9, Vieweg Verlag, (1984).

81. Diekkämper, R., "Vectorized Finite Element Analysis of Nonlinear Problems in Structural Dynamics", pp. 293–298, in Proc. Parallel Computing '83 (M. Feilmeier, G. Joubert and U. Schendel, eds), North Holland (1984).

82. Löhner, R., and Morgan, K., "Finite Element Methods on Supercomputers: The Scatter Problem", Proc. NUMETA'85 Conf. (J. Middleton and G. Pande, eds), 987–990, A.A. Balkema, Rotterdam, 1985.

83. Löhner, R., Morgan, K., and Zienkiewicz, O.C., "Effecting Programming of Finite Element Methods for CFD on Supercomputers", pp. 117–125 in The Efficient Use of Vector Computers with Emphasis on CFD (W. Schöhauer and W. Gentzsch, eds), Vieweg Notes on Numerical Fluid Mechanics, Vol. 9, Vieweg Verlag (1985).

84. Boris, J.P., "Supercomputing at the U.S. Naval Research Laboratory", Chapter in **Optical and Hybrid Computing** (H. Szu, ed), SPIE Publication, Seattle, WA (1986).

85. Boris, J.P., Reusser, E., and Young, T.R., "The Graphical and Array Processing System (GAPS)", NRL–Memo–Rpt. (1986).

86. Hinze, J.O., **Turbulence, 2nd ed.**, Chapter 2, McGraw–Hill, New York (1975).

87. Bradshaw, P., **Turbulence, Topics in Applied Physics, Vol. 12**, Springer–Verlag, New York, (1976).

88. Bradshaw, P., Cebeci, T., and Whitelaw, J.H., **Calculation Methods for Turbulent Flows**, Academic Press, New York, (1981).

89. Cebeci, T., and Smith, A.M.O., **Analysis of Turbulent Boundary Layer**, Academic Press, New York (1974).

90. Libby, P.A. and Williams, F.A., "Turbulent Reacting Flows", Topics in Applied Physics, Vol. 44, Springer–Verlag, New York (1980)

91. Jones, W.P., and Whitelaw, J.H., "Calculation Methods for Reacting Turbulent Flows: A Review", Combustion and Flame, Vol. 48, 1–26 (1982).

92. Launder, B.E., Reece, G.J., and Rodi, W., "Progress in the Development of a Reynolds Stress Turbulence Closure" J. Fluid Mech., Vol 68, 537–586 (1975).

93. Janika, J., and Kollmann, W., "A Prediction Model for Turbulent Diffusion Flames Including NO Formation", AGARD Proc. No. 275 (1980).

94. Bilger, R.W., "Perturbation Analysis of Turbulent, Non–Premixed Combustion", Comb. Sci. Tech., Vol. 22, 251 (1980).

95. Bilger, R.W., "Turbulent Flows in Non–Premixed Reactants", Turbulent Reacting Flows (P.A. Libby and F.A. Williams, eds), Ch. 3, pp. 65–114, Topics in Applied Physics, Springer–Verlag, New York, (1980).

96. Pope, S.B., "A Monte Carlo Method for the pdf Equations of Turbulent Reactive Flow", Comb. Sci. and Tec., Vol. 25, 159 (1981).

97. Spalding, D.B., "The Influence of Laminar Transport and Chemical Kinetics on the Time–Mean Reaction Rate in Turbulent Flow", 17th Sympos. (Int.) on Combustion, 431 (1978).

98. Spalding, D.B., "Concentration Fluctuations on a Round Turbulent Free Jet", Chem. Eng. Sci., Vol. 26, 95 (1971).

99. Bray, K.N.C., and Moss. J.B., "A Unified Statistical Model of the Premixed Turbulent Flame", Acta Astronautica, Vol 4, 291–319, (1977).

100. Libby, P.A., and Bray, K.N.C., "Implications of the Laminar Flamelet Model in Premixed Turbulent Combustion", Comb. Flame, Vol. 39, 33 (1980).

101. Chorin, A.J., Ghoniem, A.F., and Oppenheim, A.K., "Numerical Modeling of Turbulent Flow in Premixed Combustion", presented at the 18th Symposium (Int.) on Combustion (1981).

102. Chung, T.J., Kim, Y.M., and Sohn, J.L., "Numerical Modeling of Combustion Phenomena", Int. J. Num. Meth. Fluids, John Wiley & Sons, Inc. (1987).

103. Chung, T.J. and Lee, S.K., "Mixed spectral Finite Element Method in Spray Combustion", SIAM Conf. on Num. Comb., San Francisco, March 1987.

104. Chung, T.J., and Lee, S.K., "Droplet Vaporization Calculations Using Lagrangian Coordinate Finite Elements", AIAA–87–1983, 1987.

105. Chung, T.J., and Kim, Y.M., "Turbulent Combustion Analysis Using Finite Elements", AIAA–87–1805, 1987.

106. Chung, T.J., and Hooks, C., "Discontinuous Trial and Test Functions in Full Potential Equations", Proc. Int. Symposium on Innovative Numerical Analysis in Engineering and Applied Sciences, Versailles, France, May 23–27 (1977).

107. Heinrich, J.C., Huyakorn, P.S., Zienkiewicz, O.C., and Mitchell, A.R., "An Upwind Finite Element Scheme for Two–Dimensional Convective Transport Equation", Int. J. Num. Meth. Eng., Vol. 11, 131–144, (1977).

108. Brooks, A.N., and Hughes, T.J.R., "Streamline Upwind/Petrov–Galerkin Formulations for Convection Dominated Flows with Particular Emphasis on the Incompressible Navier–Stokes Equations", Comp. Meth. Appl. Mech. Eng., Vol. 32, 199–259 (1982).

109. Hughes, T.J.R., Franca, L.P., and Mallet, M., "A New Finite Element Formulation for Computational Fluid Dynamics: I. Symmetric Forms of the Compressible Euler and Navier–Stokes Equations and the Second Law of Thermodynamics", Comp. Meth. Appl. Mech. Eng., Vol. 54, 223–234 (1986).

110. Hughes, T.J.R., Mallet, M., and Mitzukami, A., "A New Finite Element Formulation for Computational Fluid Dynamics: II. Beyond SUPG", Comp. Meth. Appl. Mech. Eng., Vol. 54, 341–355 (1986).

111. Hughes, T.J.R., and Tezduyar, T.E., "Finite Element Methods for First–Order Hyperbolic Systems with Particular Emphasis on the Compressible Euler Equations", Comp. Meth. Appl. Mech. Eng., Vol. 45, 217–284 (1984).

112. van Leer, B., "Towards the Ultimate Conservative Scheme. II. Monotonicity and Conservation in a Second Order Scheme", J. Comp. Phys., Vol. 14, 361–370 (1974).

113. Roe, P.L., "Approximate Riemann Solvers, Parameter Vectors and Difference Schemes", J. Comp. Phys., Vol. 43, 357–372 (1981).

114. Osher, S., and Soloman, F., "Upwind Difference Schemes for Hyperbolic Systems of Conservation Laws", Math. Comp., Vol. 38, 339–374 (1982).

115. Hawthorne, W.R., Weddell, D.S., and Hottel, H.C., "Mixing and Combustion in Turbulent Gas Jets", Third Symposium on Combustion, Flame, and Explosion Phenomena, 266–288 (1949).

116. Kent, J.H., and Bilger, R.W., "The Prediction of Turbulent Diffusion Flame Fields and Nitric Oxide Formation", 16th Symposium (Int) on Combustion, 1643–1656 (1977).

117. Kennedy, I.M., and Kent, J.H., "Measurements of a Conserved Scalar in Turbulent Jet Diffusion Flames", 17th Symposium (Int) on Combustion, 279–287 (1979).

118. Gibson, C.H., and Libby, P.A., Vol. 6, 29, Combustion Sci. and Tech. (1972).

119. Bilger, R.W., and Beck, R.E>, "Further Experiments in Turbulent Jet Diffusion Flames", 15th Symposium (Int) on Combustion, 541 (1975).

120. Janicka, J., and Kollman, W., "A Two–Variables Formalism for the Treatment of Chemical Reactions in Turbulent H_2–Air Diffusion Flames, 17th Symposium (Int) on Combustion, 421–430 (1979).

121. Borghi, R., "Chemical Calculations in Turbulent Flows – Application to CO Containing Turbojet Flame", Adv. Geophys., Vol. 18B, 349 (1974).

122. Hutchinson, P., Khalil, E.E., and Whitelaw, J.H., **Turbulent Combustion** (L.A. Kennedy, Ed), Progress in Astronautics and Aeronautics, Vol. 58, 211 (1978).

123. Kaskan, W.E., and Schott, G.L., **Combustion and Flame**, Vol. 6, 73 (1962).

124. Donaldson, C. duP., and Varma, A.K., "Remarks on Construction of a Second–Order Closure Description of Turbulent Reacting Flows", Comb. Sci. and Tech., Vol 13, 55–78 (1976).

125. Lundgren, T.S., "Distribution Functions in Statistical Theory of Turbulence", Phys. Fluids, Vol 10, 969–975, (1967).

126. Monin, A.S., "Equations of Turbulent Motion:, Prikl. Mat. Mekh., Vol 31, 1057–1067 (1967).

127. Monin, A.S., "Equations for Finite Dimensional Probability Distributions of a Field of Turbulence", Dokl. Adad. Nawk SSSR, Vol 177, 1036–1038 (1967).

128. O'Brien, E.E., "Statistical Methods in Reacting Turbulent Flows", AIAA Paper 80–0137, presented at 18th AIAA Aerospace Sciences Meeting, January 14–16 (1980).

129. Dopazo, C., **Nonisothermal Turbulent Reactive Flows: Stochastic Approaches**, PhD Dissertation, State University of New York at Stony Brook (1973).

130. Dopazo, C., "Probability Density Function Approach for a Turbulent Axisymmetric Heated Jet: Centerline Evolution", Phys. Fluids, Vol 18, 397–404 (1975).

131. Dopazo, C., "A Probabilistic Approach to Turbulent Flame Theory", Acta Astronautica, Vol 3, 853–878 (1976).

132. Peters, N., Vol 30, No. 2, Combustion Science and Tech., (1983).

133. Peters, N., "Laminar Diffusion Flamelet Models in Nonpremixed Turbulent Combustion", Progress in Energy and Combustion Sci. (1983).

134. Ghoniem, A.F., Chen, D.Y., and Oppenheim, A.K., "Formation and Inflammation of a Turbulent Jet", published in AIAA Journal (1985).

135. Cantrell, R.H., and Hart, R.W., "Interaction Between Sound and Flow in Acoustic Cavities: Mass, Momentum, and Energy Considerations," Journal of Acous. Soc. Amer., Vol. 36, No. 4, pp. 697–706, 1964.

136. Culick, F.E.C., "Stability of Three–Dimensional Motions in a Combustion Chamber," Combustion Science and Technology, Vol. 10, pp. 109–124, 1975.

137. Sirignano, W.A., and Crocco, L., "A Shock Wave Model of Unstable Rocket Combustion," AIAA Journal, Vol. 2, No. 7, p. 1285, July 1964.

138. Harvje, D.T., and Reardon, F.H., Ed., "Liquid Propellant Rocket Combustion Instability," NASA SP–194, 1972.

139. Baum, J.D., and Levine, J.N., "Modeling of Nonlinear Combustion Instability in Solid Propellant Rocket Motors," AFRPL TR–83–058, February 1984.

140. Chung, T.J., and Sohn, J.L., "Interactions of Coupled Acoustic and Vortical Instability," AIAA Journal, Vol. 24, No. 10, pp. 1582–1595, 1982.

141. Michalke, A., "On the Inviscid Instability of the Hyperbolic Tangent Velocity Profiles," Journal of Fluid Mechanics, Vol. 9, pp. 543–556, 1964.

142. Michalke, A., "Vortex Formation in a Free Boundary Layer According to Stability Theory," Journal of Fluid Mechanics, Vol. 22, Pt. 2, 1965.

143. Michalke, A., "On Spatially Growing Disturbances in an Inviscid Shear Layer," Journal of Fluid Mechanics, Vol. 25, Pt. 4, pp. 521–554, 1966.

144. Williams, F.A., "Combustion Theory," The Benjamin/Cummings Publishing Co., 2nd Ed., 1985.

145. Flandro, G.A., "Energy Balance Analysis of Nonlinear Combustion Instability," AIAA Journal of Propulsion, Vol. 1, No. 3, pp. 210–221, 1985.

146. Kim, Y.M., and Chung, T.J., "Finite Element Analysis of Turbulent Diffusion Flames," AIAA Journal, Vol. 27, No. 3, pp 330–339, 1989.

147. Spradley, L.W., Stalnaker, J.F., and Löhner, R., "Finite Element Code for Combustion Analysis of Advanced Propulsion Systems," Final Report, SBIR, NAS8–38022, 1989.

148. Yoon, W.S., Chung, T.J., Stalnaker, J.F., and Spradley, L.W., "Analysis of Unstable Nonlinear Combustion Waves Using Entropy Controlled Instability (ECI) Method", AIAA paper, AIAA90–2362, July 1990.

149. Donea, J., "A Taylor–Galerkin Method for Convective Transport Problems", Int. J. Num. Meth. Engng., 20, pp. 101–119, 1984.

150. Löhner, R., "A Finite Element Solver for Axisymmetric Compressible Flows", AIAA Paper 89–1794, June 12–14, 1989.

151. Chung, T.J., Finite Element Analysis in Fluids and Heat Transfer, Krieger Publishing Company, 1991.

152. Clark, W.H., Crump, J.E., and Mathes, H.B., "Results of Tests for Nonlinear Stability of Full Scale Rocket Motors", 25th JANNAF Combustion Meeting, 1988.

APPENDIX A

INTEGRANDS OF E_1, E_2, E_3, I_1, I_2, I_3

$$a^{(1)} = \frac{\bar{\rho}}{2} v_j' v_j' + \rho' \bar{v}_j v_j'$$

$$a^{(2)} = \frac{1}{2} \rho' v_j' v_j'$$

$$a^{(3)} = -\frac{1}{\gamma-1} \left(\frac{\bar{p}\rho'^4}{\bar{\rho}^4}\right)$$

$$b^{(1)} = \bar{\rho}\bar{v}_i \left(-\frac{p'\rho'}{(\gamma-1)\bar{\rho}^2} + \frac{\bar{p}\,\rho'^2}{(\gamma-1)\bar{\rho}^3} + \frac{1}{2} v_j' v_j'\right)_{,i} + (\bar{\rho} v_i' + \bar{v}_i \rho')\left(\frac{p'}{(\gamma-1)\bar{\rho}} - \frac{\bar{p}\rho'}{(\gamma-1)\bar{\rho}^2}\right.$$

$$\left. + \bar{v}_j v_j'\right)_{,i} + v_i' \rho' \left(\frac{\bar{p}}{(\gamma-1)\bar{\rho}} + \frac{1}{2} \bar{v}_j \bar{v}_j\right)_{,i} + \bar{\rho}\left(-\frac{\bar{v}_i p' \rho'}{\bar{\rho}^2} + \frac{\bar{v}_i \bar{p}}{\bar{\rho}^3} \rho'^2 + \frac{p' v_i'}{\bar{\rho}} - \frac{\bar{p} v_i' \rho'}{\bar{\rho}^2}\right)_{,i}$$

$$+ \rho'\left(\frac{\bar{v}_i p'}{\bar{\rho}} - \frac{\bar{p}\bar{v}_i \rho'}{\bar{\rho}^2} + \frac{\bar{p} v_i'}{\bar{\rho}}\right)_{,i} + \left(-\frac{p'^2}{2(\gamma-1)\bar{p}^2} + \frac{\gamma\rho'^2}{2(\gamma-1)\bar{\rho}^2}\right)(\bar{p}\bar{v}_i)_{,i} + \left(\frac{p'}{(\gamma-1)\bar{p}} - \frac{\gamma\rho'}{(\gamma-1)\bar{\rho}}\right)$$

$$(\bar{p} v_i' + p' \bar{v}_i)_{,i} + \bar{v}_j \left(\bar{\rho} v_i' v_j' + \rho' \bar{v}_j v_i' + \rho' \bar{v}_i v_j'\right)_{,i} + v_j' \left(\bar{\rho}\bar{v}_i v_j' + \bar{\rho} v_i' \bar{v}_j + \rho' \bar{v}_i \bar{v}_j\right)_{,i}$$

$$- \lambda(T')_{,i} T'_{,i} + \left(\bar{\rho}\, D \sum_{k=1}^{N} c_{pk} T'\right)_{,i} Y_{k,i}' + \left(\rho'\, D \sum_{k=1}^{N} c_{pk} \bar{T}\right)_{,i} Y_{k,i}' + \left(\rho'\, D \sum_{k=1}^{N} c_{pk} T'\right)_{,i} \bar{Y}_{k,i}$$

$$b^{(2)} = (\bar{\rho} v_i' + \bar{v}_i \rho')\left(-\frac{p'\rho'}{(\gamma-1)\bar{\rho}^2} + \frac{\bar{p}\rho'^2}{(\gamma-1)\bar{\rho}^3} + \frac{1}{2} v_j' v_j'\right)_{,i} + \rho' v_i' \left(\frac{p'}{(\gamma-1)\bar{\rho}} - \frac{\bar{p}\rho'}{(\gamma-1)\bar{\rho}^2}\right.$$

$$\left. + \bar{v}_j v_j'\right)_{,i} + \bar{\rho}\bar{v}_i \left(\frac{p'\rho'^2}{(\gamma-1)\bar{\rho}^3} - \frac{\bar{p}\rho'^3}{(\gamma-1)\bar{\rho}^4}\right)_{,i} + \bar{\rho}\left(\frac{\bar{v}_i p'\rho'^2}{\bar{\rho}^3} - \frac{\bar{v}_i \bar{p}\rho'^3}{\bar{\rho}^4} - \frac{v_i' p'\rho'}{\bar{\rho}^2} + \frac{\bar{p} v_i' \rho'^2}{\bar{\rho}^3}\right)_{,i}$$

$$+ \rho'\left(-\frac{\bar{v}_i p'\rho'}{\bar{\rho}^2} + \frac{\bar{v}_i \bar{p}\rho'^2}{\bar{\rho}^3} + \frac{p' v_i'}{\bar{\rho}} - \frac{\bar{p} v_i' \rho'}{\bar{\rho}^2}\right)_{,i} + \left(\frac{p'^3}{3(\gamma-1)\bar{p}^3} - \frac{\gamma\rho'^3}{3(\gamma-1)\bar{\rho}^3}\right)(\bar{p}\bar{v}_i)_{,i}$$

$$+ \left(-\frac{p'^2}{2(\gamma-1)\bar{p}^2} + \frac{\gamma\rho'^2}{2(\gamma-1)\bar{\rho}^2}\right)(\bar{p} v_i' + p' \bar{v}_i)_{,i} + \left(\frac{p'}{(\gamma-1)\bar{p}} - \frac{\gamma\rho'}{(\gamma-1)\bar{\rho}}\right)(p' v_i')_{,i}$$

$$+ \left(\rho'\, D \sum_{k=1}^{N} c_{pk} T'\right)_{,i} Y_{k,i}' + \bar{v}_j \left(\rho' v_i' v_j'\right)_{,i} + v_j' \left(\bar{\rho} v_i' v_j' + \bar{v}_i \rho' v_j' + \bar{v}_j \rho' v_i'\right)_{,i}$$

$$b^{(3)} = \bar{\rho}\bar{v}_i\left(-\frac{p'\rho'^3}{(\gamma-1)\bar{\rho}^4}\right)_{,i} + (\bar{\rho}v_i' + \bar{v}_i\rho')\left(\frac{p'\rho'^2}{(\gamma-1)\bar{\rho}^3} - \frac{\bar{p}\rho'^3}{(\gamma-1)\bar{\rho}^4}\right)_{,i} + \rho' v_i'\left(-\frac{p'\rho'}{(\gamma-1)\bar{\rho}^2} + \frac{\bar{p}\rho'^2}{(\gamma-1)\bar{\rho}^3}\right.$$

$$\left. + \frac{1}{2}v_j'v_j'\right)_{,i} + \bar{\rho}\left(\frac{v_i'p'\rho'^2}{\bar{\rho}^3} - \frac{\bar{p}v_i'\rho'^3}{\bar{\rho}^4} - \frac{\bar{v}_i p'\rho'^3}{\bar{\rho}^4}\right) + \rho'\left(\frac{\bar{v}_i p'\rho'^2}{\bar{\rho}^3} - \frac{\bar{p}\bar{v}_i\rho'^3}{\bar{\rho}^4} - \frac{v_i'p'\rho'}{\bar{\rho}^2} + \frac{\bar{p}v_i'\rho'^2}{\bar{\rho}^3}\right)_{,i}$$

$$+ \left(\bar{p}\bar{v}_i\right)_{,i}\left(-\frac{p'^4}{4(\gamma-1)\bar{p}^4} + \frac{\gamma\rho'^4}{4(\gamma-1)\bar{\rho}^4}\right) + \left(\bar{p}v_i' + p'\bar{v}_i\right)_{,i}\left(\frac{p'^3}{3(\gamma-1)\bar{p}^3} - \frac{\gamma\rho'^3}{6(\gamma-1)\bar{\rho}^3}\right)$$

$$+ (p'v_i')_{,i}\left(-\frac{p'^2}{2(\gamma-1)\bar{p}^2} + \frac{\gamma\rho'^2}{2(\gamma-1)\bar{\rho}^2}\right) + \left(\rho' v_i'v_j'\right)_{,i}v_j'$$

$$c_i^{(1)} = \bar{\rho}\bar{v}_i\left(-\frac{p'\rho'}{(\gamma-1)\bar{\rho}^2} + \frac{\bar{p}\rho'^2}{(\gamma-1)\bar{\rho}^3} + \frac{1}{2}v_j'v_j'\right) + \left(\bar{\rho}v_i' + \bar{v}_i\rho'\right)\left(\frac{p'}{(\gamma-1)\bar{\rho}} - \frac{\bar{p}\rho'}{(\gamma-1)\bar{\rho}^2} + \bar{v}_j v_j'\right)$$

$$\rho' v_i'\left(\frac{\bar{p}}{(\gamma-1)\bar{\rho}} + \frac{1}{2}\bar{v}_j\bar{v}_j\right) + p'v_i' + \left(-\frac{p'^2}{2(\gamma-1)\bar{p}^2} + \frac{\gamma\rho'^2}{2(\gamma-1)\bar{\rho}^2}\right)\bar{p}\bar{v}_i + \left(\frac{p'}{\gamma-1)\bar{p}} - \frac{\gamma\rho'}{(\gamma-1)\bar{\rho}}\right)\left(\bar{p}v_i'\right.$$

$$\left. + p'\bar{v}_i\right) + \bar{v}_i\left(\bar{\rho}v_j'v_j' + 2\rho'\bar{v}_j v_j'\right) + v_i'\left(2\bar{\rho}\bar{v}_j v_j' + \rho'\bar{v}_j\bar{v}_j\right) + v_j'\left[p'\delta_{ij} - \mu\left(v_{i,j}' + v_{j,i}'\right)\right]$$

$$+ \frac{2}{3}\mu\, v_{k,k}'v_i' - \left(\lambda(T')\right)T'_{,i} + \bar{\rho}\, D\sum_{k=1}^{N} c_{pk}T'Y_{k,i}' + \rho'\, D\sum_{k=1}^{N} c_{pk}\bar{T}\, Y_{k,i}' + \rho' D\sum_{k=1}^{N} c_{pk}T'Y_{k,i}'$$

$$c_i^{(2)} = \left(\bar{\rho}v_i' + \bar{v}_i\rho'\right)\left(-\frac{p'\rho'}{(\gamma-1)\bar{\rho}^2} + \frac{\bar{p}\rho'^2}{(\gamma-1)\bar{\rho}^3} + \frac{1}{2}v_j'v_j'\right) + \rho' v_i'\left(\frac{p'}{(\gamma-1)\bar{\rho}} - \frac{\bar{p}\rho'}{(\gamma-1)\bar{\rho}^2} + \bar{v}_j v_j'\right)$$

$$+ \bar{\rho}\bar{v}_i\left(\frac{p'\rho'^2}{(\gamma-1)\bar{\rho}^3} - \frac{\bar{p}\,\rho'^3}{(\gamma-1)\bar{\rho}^4}\right) + \left(\frac{p'^3}{3(\gamma-1)\bar{p}^3} - \frac{\gamma\rho'^3}{3(\gamma-1)\bar{\rho}^3}\right)\bar{p}\bar{v}_i + \left(\frac{p'^2}{2(\gamma-1)\bar{p}^2} - \frac{\gamma\rho'^2}{2(\gamma-1)\bar{\rho}^2}\right)\left(\bar{p}v_i'\right.$$

$$\left. + p'\bar{v}_i\right) + \left(\frac{p'}{(\gamma-1)\bar{p}} - \frac{\gamma\rho'}{(\gamma-1)\bar{\rho}}\right)p'v_i' + \rho'\bar{v}_i v_j'v_j' + \bar{\rho}v_i'v_j'v_j' + 2\rho' v_i'\bar{v}_j v_j' + \rho' D\sum_{k=1}^{N} c_{pk}T'\, Y_{k,i}'$$

$$c_i^{(3)} = \bar{\rho}\bar{v}_i\left(-\frac{p'\rho'^3}{(\gamma-1)\bar{\rho}^4}\right) + \left(\bar{\rho}v_i' + \bar{v}_i\rho'\right)\left(\frac{p'\rho'^2}{(\gamma-1)\bar{\rho}^3} - \frac{\bar{p}\rho'^3}{(\gamma-1)\bar{\rho}^4}\right) + \rho' v_i'\left(-\frac{p'\rho'}{(\gamma-1)\bar{\rho}^2} + \frac{\bar{p}\rho'^2}{(\gamma-1)\bar{\rho}^3}\right.$$

$$\left. + \frac{1}{2}v_j'v_j'\right) + \left(\frac{p'^3}{3(\gamma-1)\bar{p}^3} - \frac{\gamma\rho'^3}{3(\gamma-1)\bar{\rho}^3}\right)\left(\bar{p}v_i' + p'\bar{v}_i\right) + \left(-\frac{p'^2}{2(\gamma-1)\bar{p}^2} + \frac{\gamma\rho'^2}{2(\gamma-1)\bar{\rho}^2}\right)p'v_i'$$

$$+ \left(-\frac{p'^4}{4(\gamma-1)\bar{p}^4} + \frac{\gamma\rho'^4}{4(\gamma-1)\bar{\rho}^4}\right)\bar{p}\bar{v}_i + \rho' v_i'v_j'v_j'$$

APPENDIX B
REACTION EQUATIONS

$H_2 + O_2 = 2OH$

$H + O_2 = OH + O$

$OH + H_2 = H_2O + H$

$O + H_2 = OH + H$

$2OH = H_2O + O$

$H + OH + M = H_2O + M$

$2H + M = H_2 + M$

$H + O_2 + M = HO_2 + M$

$HO_2 + OH = H_2O + O_2$

$HO_2 + H = H_2 + O_2$

$HO_2 + H = 2OH$

$HO_2 + O = OH + O_2$

$2HO_2 = H_2O_2 + O_2$

$HO_2 + H_2 = H_2O_2 + H$

$H_2O_2 + OH = HO_2 + H_2O$

$H_2O_2 + H = OH + HO_2$

$H_2O_2 + O = OH + HO_2$

$H_2O_2 + M = 2OH + M$

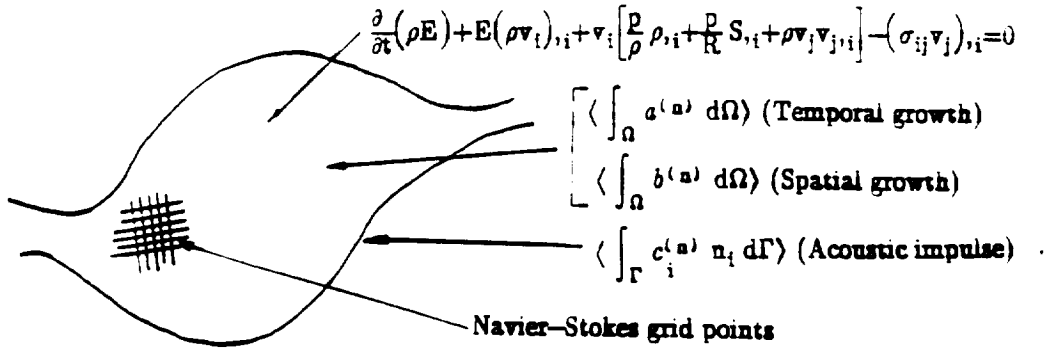

(a) Concept of ECI method

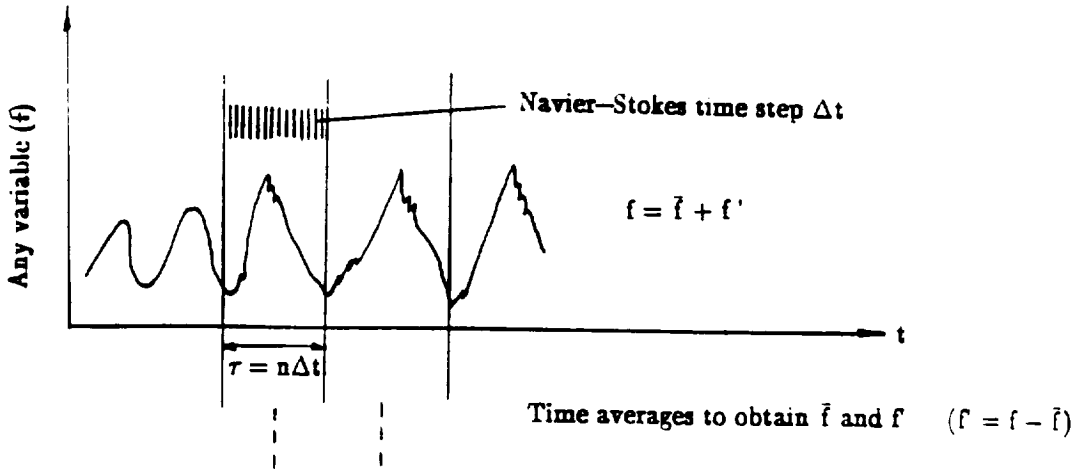

(b) Navier–Stokes solutions with initial oscillatory boundary conditions

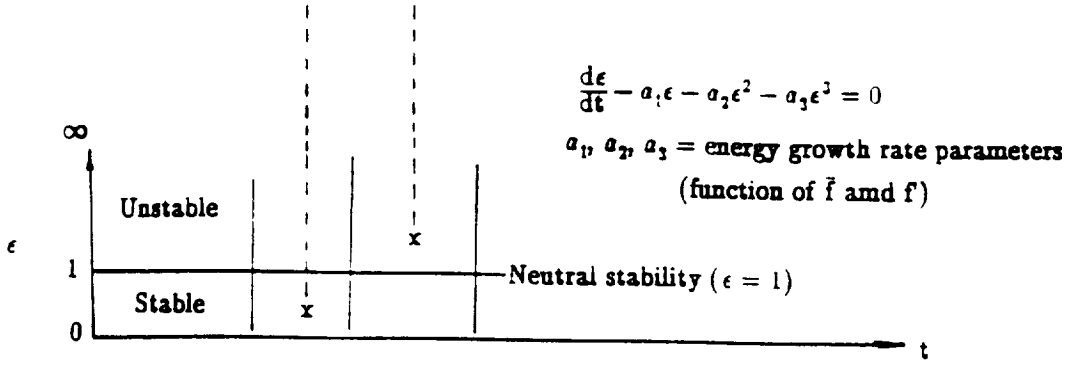

(c) Energy growth factor (ϵ)

Fig. 1 Schematic overview of ECI method

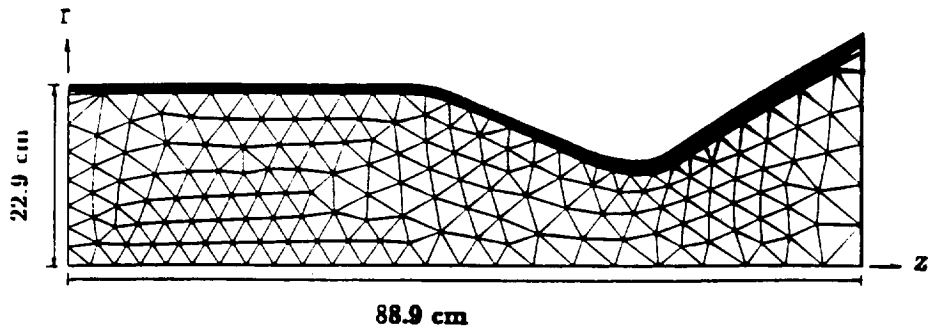

(a) Discretised geometry, 965 elements, 528 nodes

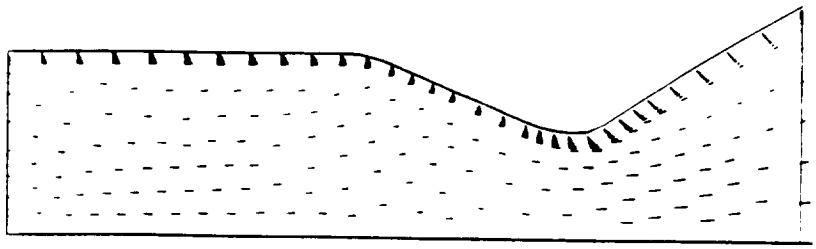

(b) Velocity field, 1 mm = 105 m/s

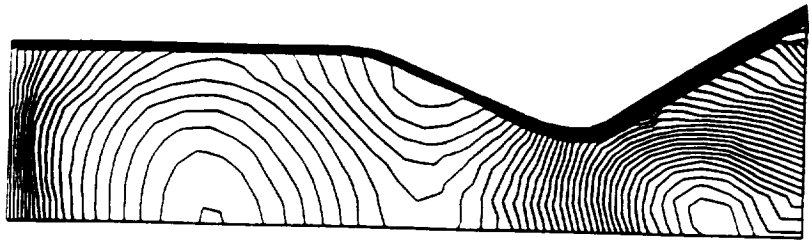

(c) Mach number contours, max = 1.6, min = 1.6, incr = 0.032

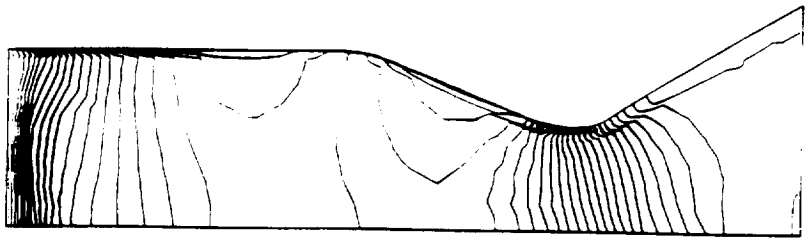

(d) Pressure contours, max = 3000 psi, min = 230 psi, incr = 53 psi

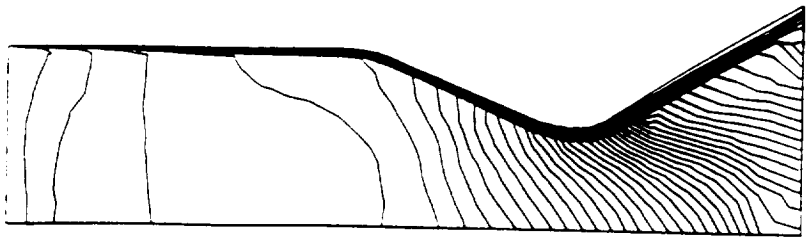

(e) Temperature contours, max = 3656.33° K, min = 8.26° K, incr = 72.96° K

Fig. 2 Steady state laminar nonreacting flow without disturbances. M (inlet) = 0.2, Re = 66,000, $\mu = 0.23$ kg/m^2/s, $\gamma = 1.2$, $\bar{p} = 3000$ psi, $\rho = 55.8$ kg/m^3, T = 3656.33° K

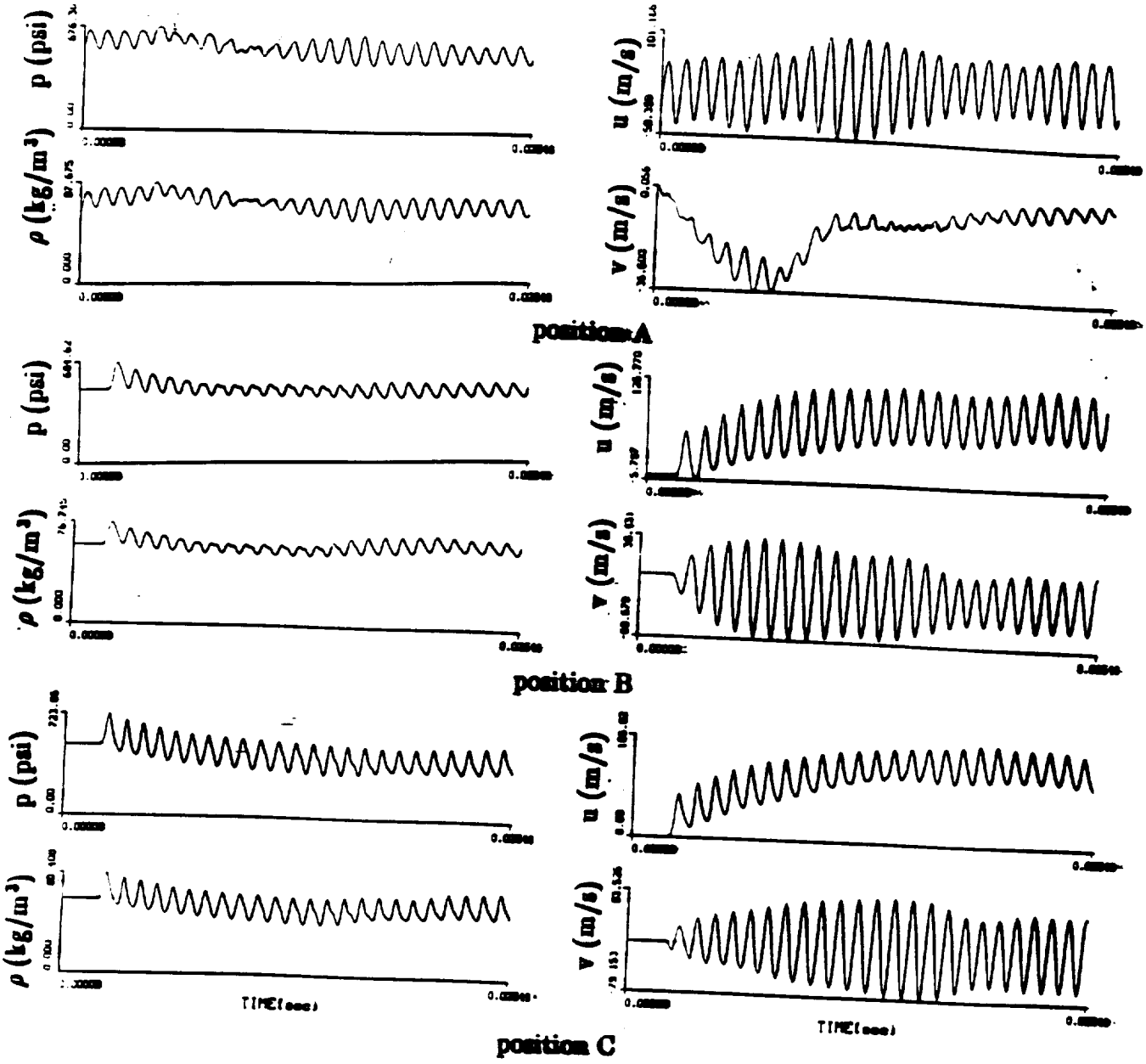

Fig. 3 **Waveforms for transient laminar nonreacting flow with disturbances. Pressure, density, axial velocity, and radial velocity vs time at various positions. Position A (1.8, 11.43 cm), position B (31.75, 11.45 cm), position C (63.5, 6.55 cm)**

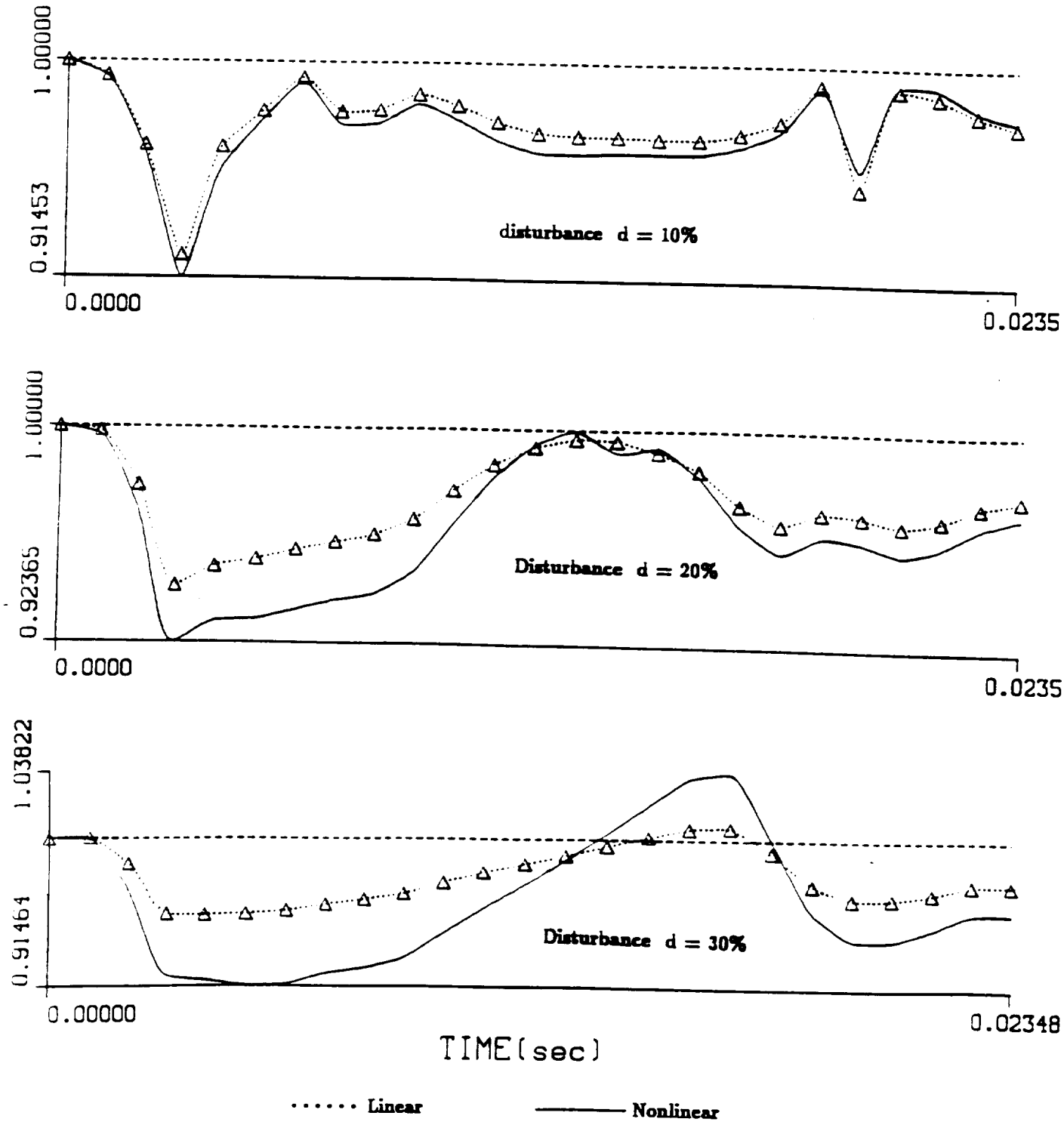

Fig. 4 Energy growth factor vs time, transient laminar flow with disturbances, $\bar{p} = 500$ psi, f (inlet) = 1022 Hz, M (inlet) = 0.2

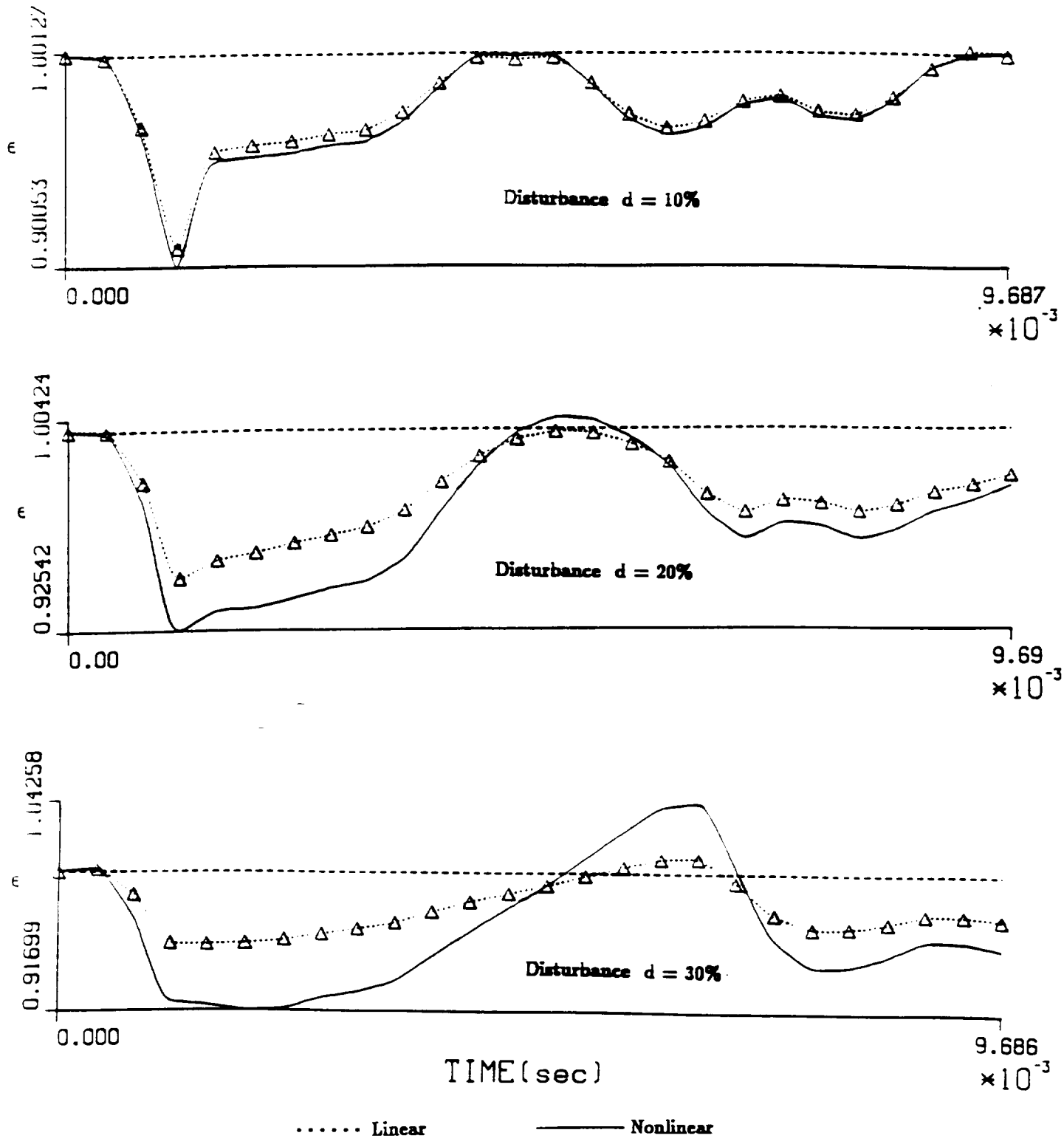

Fig. 5 Energy growth factor vs time, transient laminar flow with disturbances, $\bar{p}$ = 3000 psi, f (inlet) = 1022 Hz, M (inlet) = 0.2

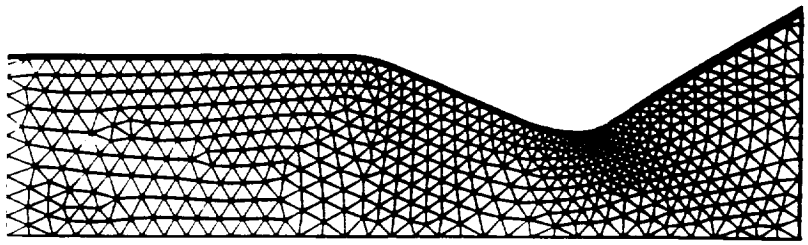

(a) Discretised geometry, 2688 elements, 1416 nodes

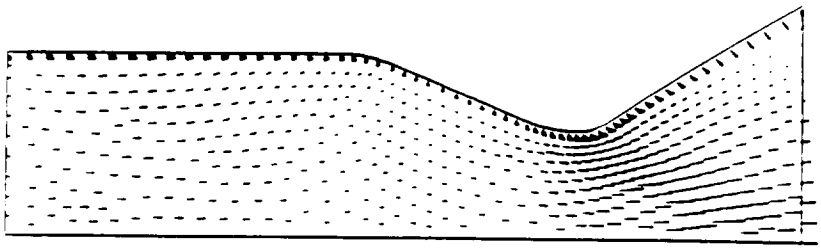

(b) Velocity field, 1 mm = 105 m/s

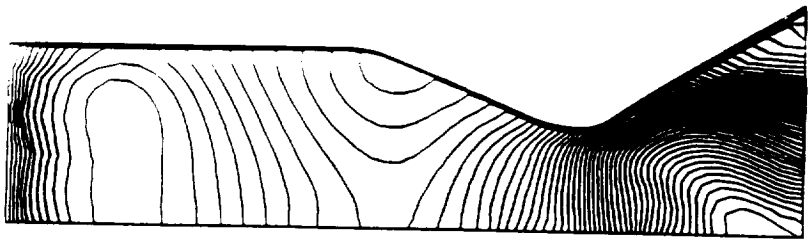

(c) Mach number contours, max = 2.2, min = 0, incr = 0.044

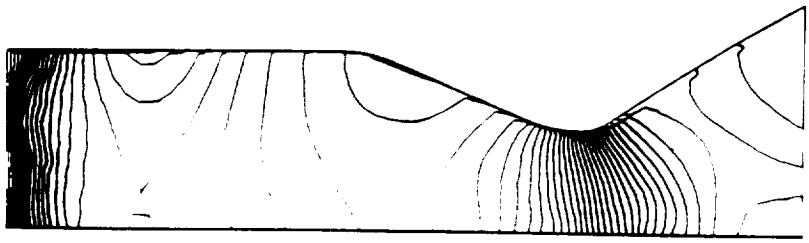

(d) Pressure contours, max = 3000 psi, min = 227 psi, incr = 54 psi

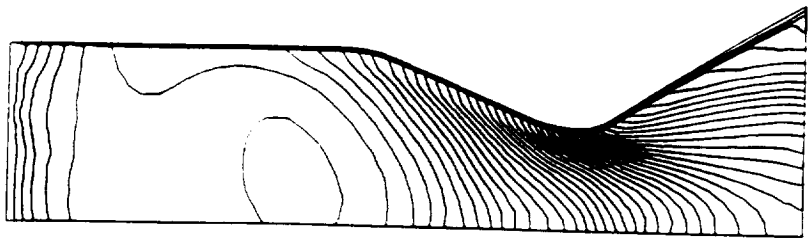

(e) Temperature contours, max = 3656.33° K, min = 15.45° K, incr = 72.82° K

Fig. 6 Steady state turbulent nonreacting flow without disturbances. M (inlet) = 0.2, Re = 500,000, $\mu = 1.737$ kg/m^2/s, $\gamma = 1.2$, $\bar{p} = 3000$ psi, $\rho = 55.8$ kg/m^3, T = 3656.33° K

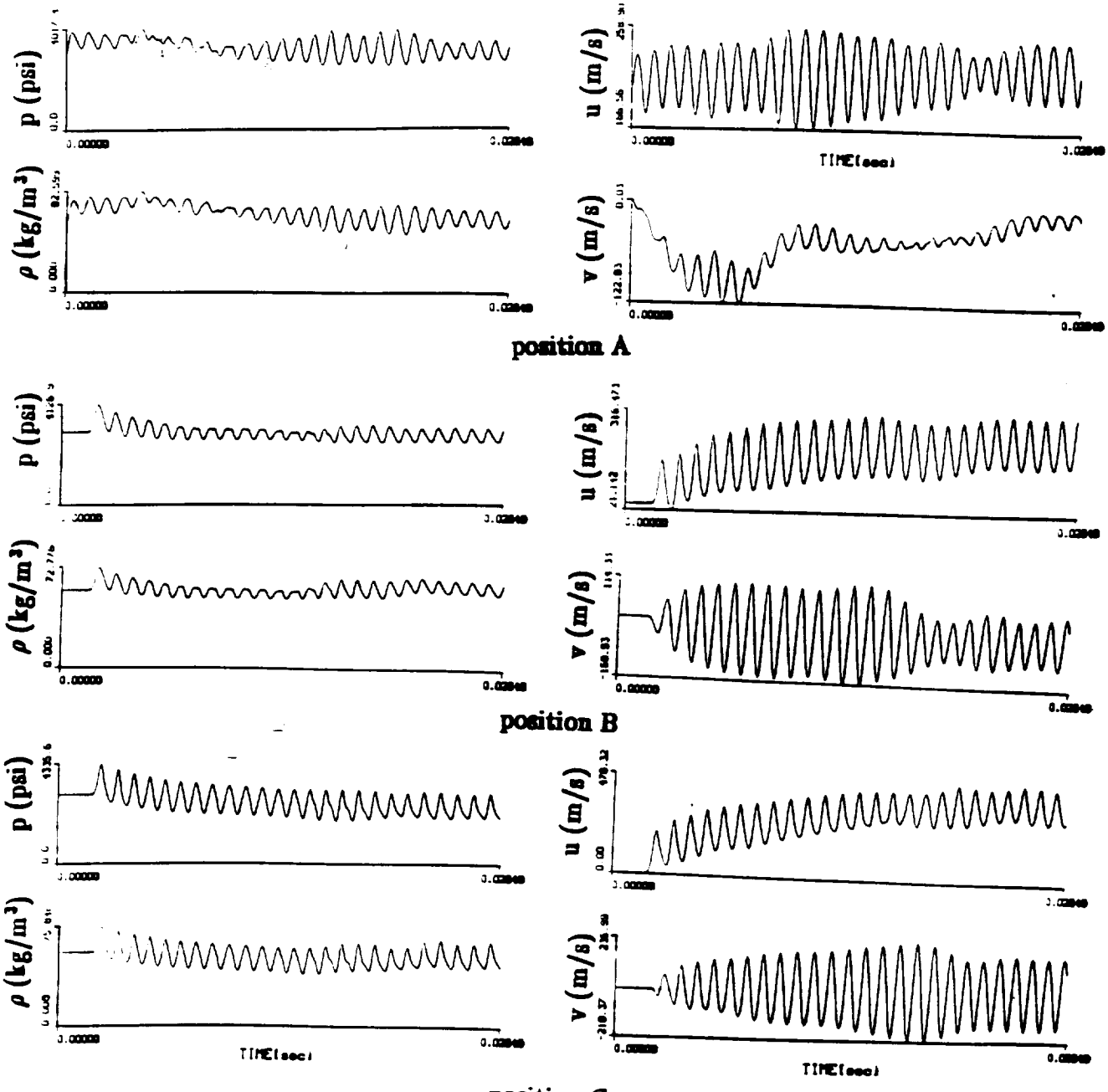

Fig. 7 Wave forms for transient turbulent flow with disturbances, pressure, density, axial velocity and radial velocity vs time at various positions. Position A (1.8, 11.43 cm), Position B (31.75, 11.45 cm), Position C (63.5, 6.55 cm)

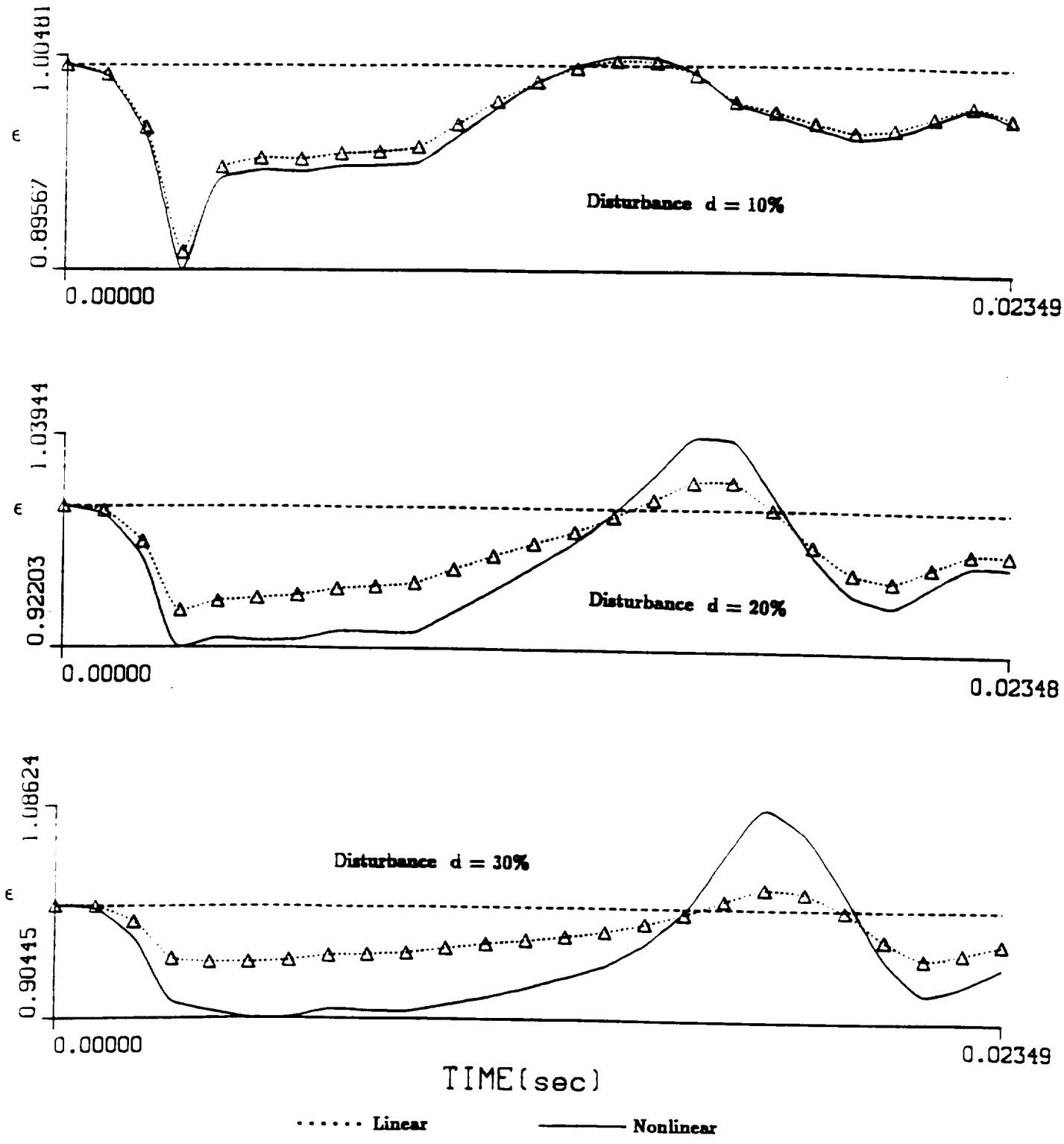

Fig. 8 Energy growth factor vs time, transient turbulent flow with disturbances, $\bar{p}$ = 500 psi, f (inlet) = 1022 Hz, M (inlet) = 0.2

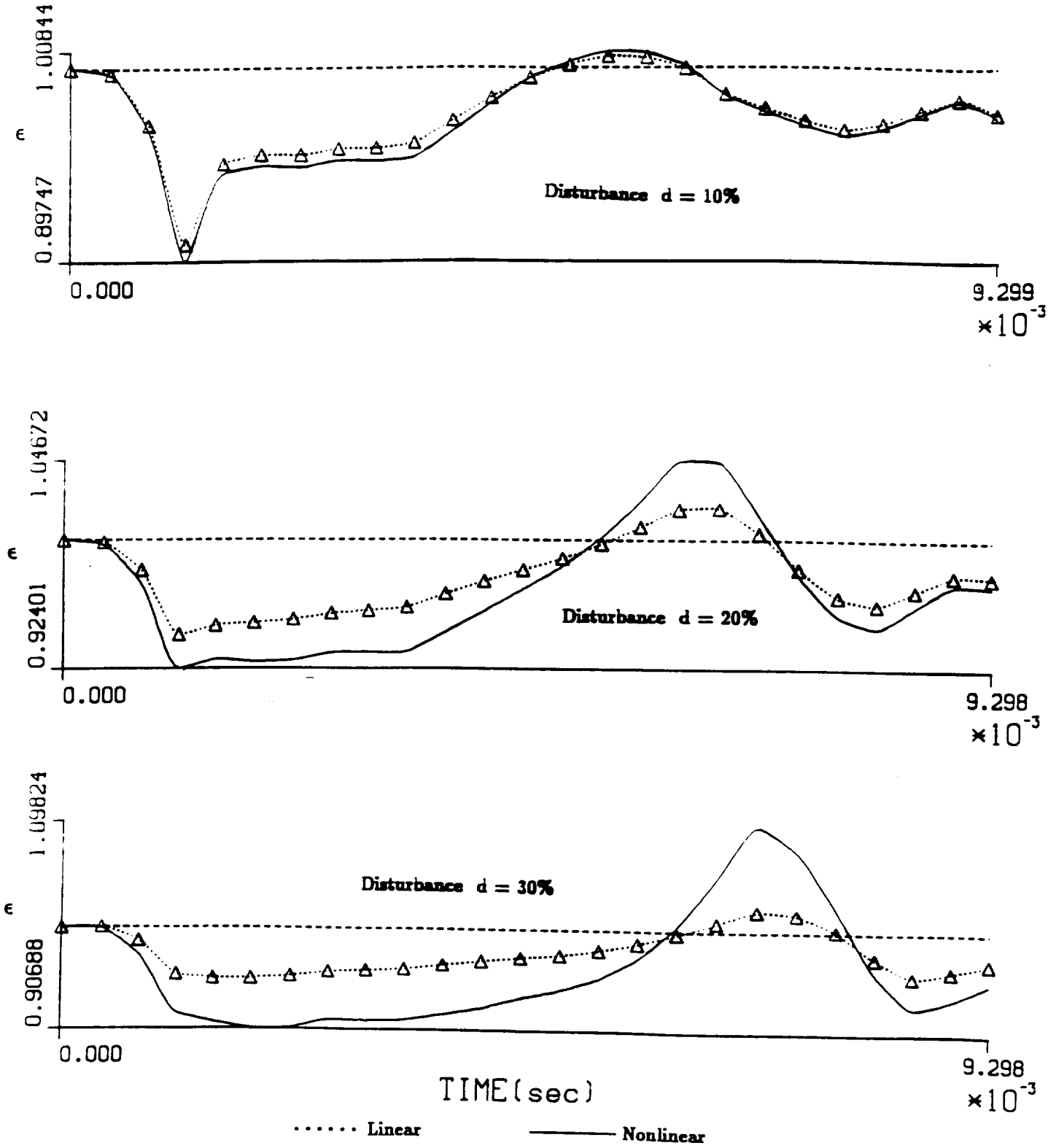

Fig. 9 Energy growth factor vs time, transient turbulent flow with disturbances, $\bar{p}$ = 3000 psi, f (inlet) = 1022 Hz, M (inlet) = 0.2

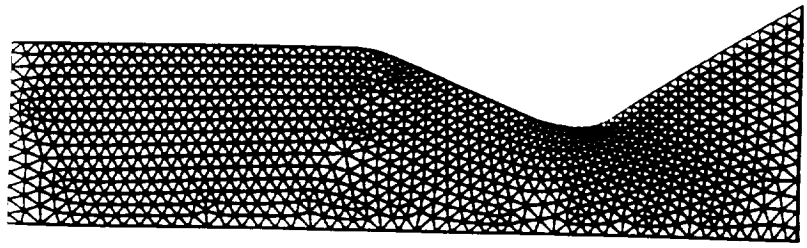

(a) Discretised geometry, 1580 elements, 844 nodes

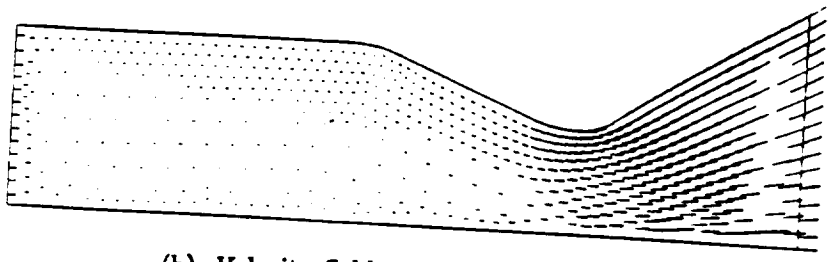

(b) Velocity field, 1 mm = 262 m/s

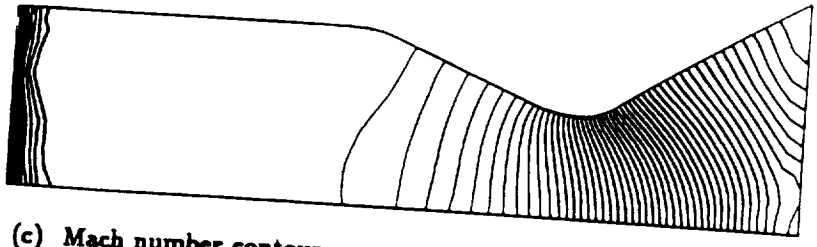

(c) Mach number contours, max = 4.8, min = 0.33, incr = 0.089

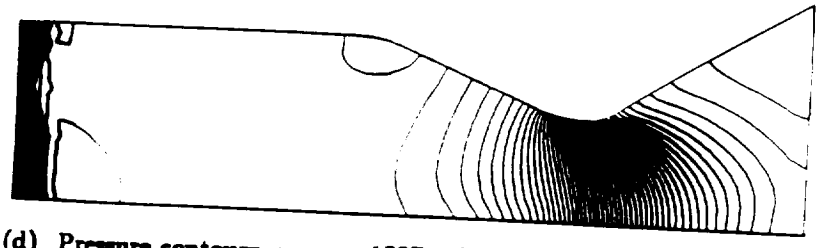

(d) Pressure contours, max = 1897 psi, min = 46 psi, incr = 37 psi

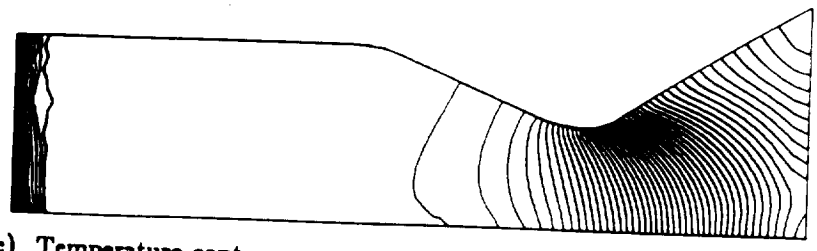

(e) Temperature contours, max = 635.1° K, min = 260.2° K, incr = 7.5° K

Fig 10 Steady state chemically reacting flow without disturbances, inlet velocity = 500 m/s, Re = 66,000, $\mu = 0$, $\gamma = 1.413$, $\bar{p} = 500$ psi, $\rho = 40.08$ kg/m^3, T = 500° K, inlet mass fraction $H_2 = 0.111$, $O_2 = 0.889$

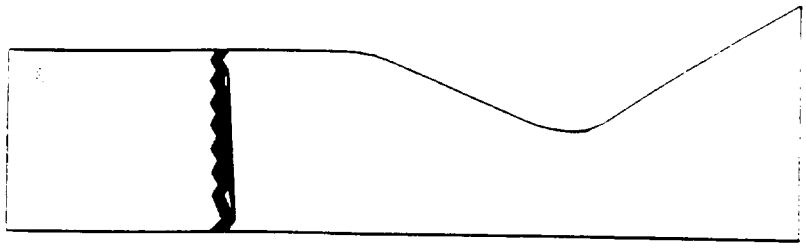

(a) H_2 contours, max = 0.111, min = 0.11, incr = 0.8×10^{-5}

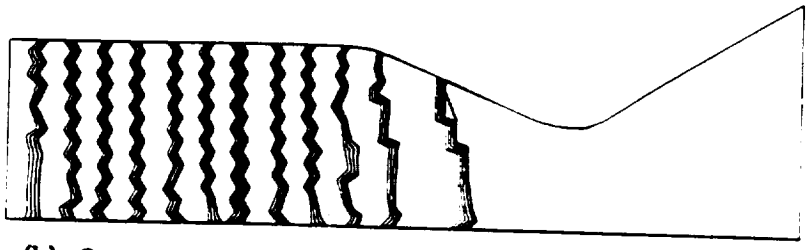

(b) O_2 contours, max = 0.889, min = 0.884, incr = 0.96×10^{-4}

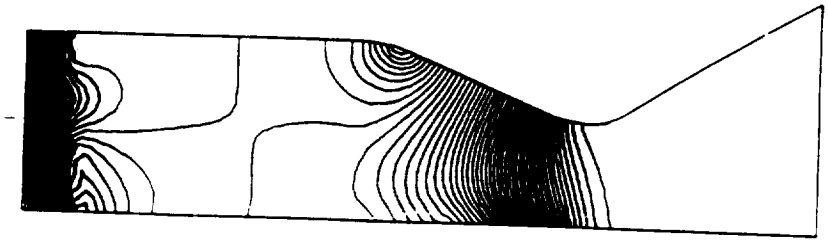

(c) H contours, max = 0.145×10^{-14}, min = 0, incr = 2.89×10^{-16}

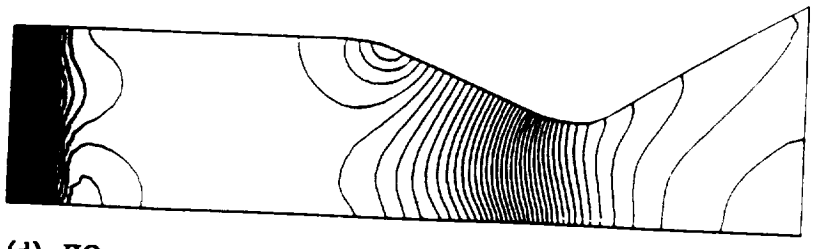

(d) HO_2 contours, max = 0.46×10^{-5}, min = 0, incr = 0.92×10^{-7}

Fig 11 Distributions of various chemical species at steady state without disturbances

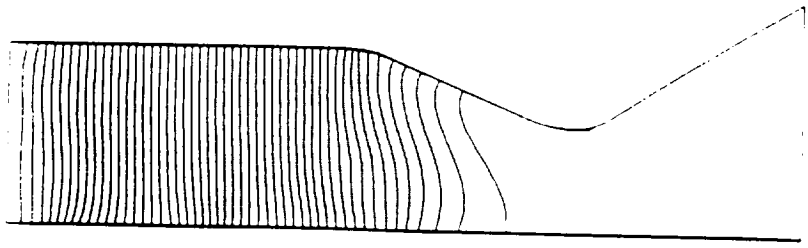

(e) H_2O contours, max = 0.0056, min = 0, incr = 0.00011

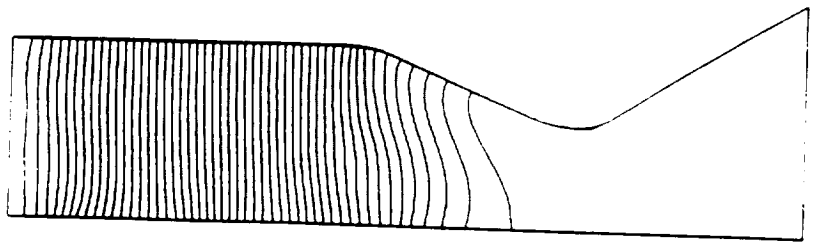

(f) H_2O_2 contours, max = 0.412×10^{-3}, min = 0, incr = 0.82×10^{-5}

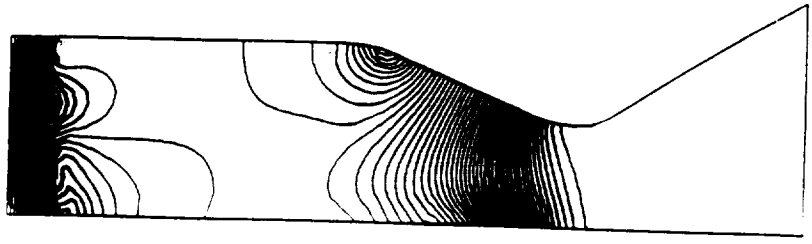

(g) O contours, max = 0.1139×10^{-11}, min = 0, incr = 0.22×10^{-13}

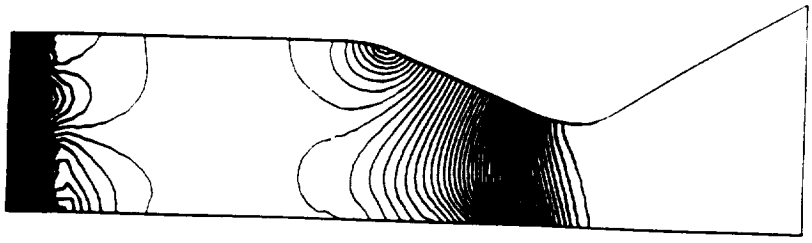

(h) OH contours, max = 0.5817×10^{-13}, min = 0, incr = 0.12×10^{-14}

Fig 11 Distributions of various chemical species at steady state without disturbances, continued.

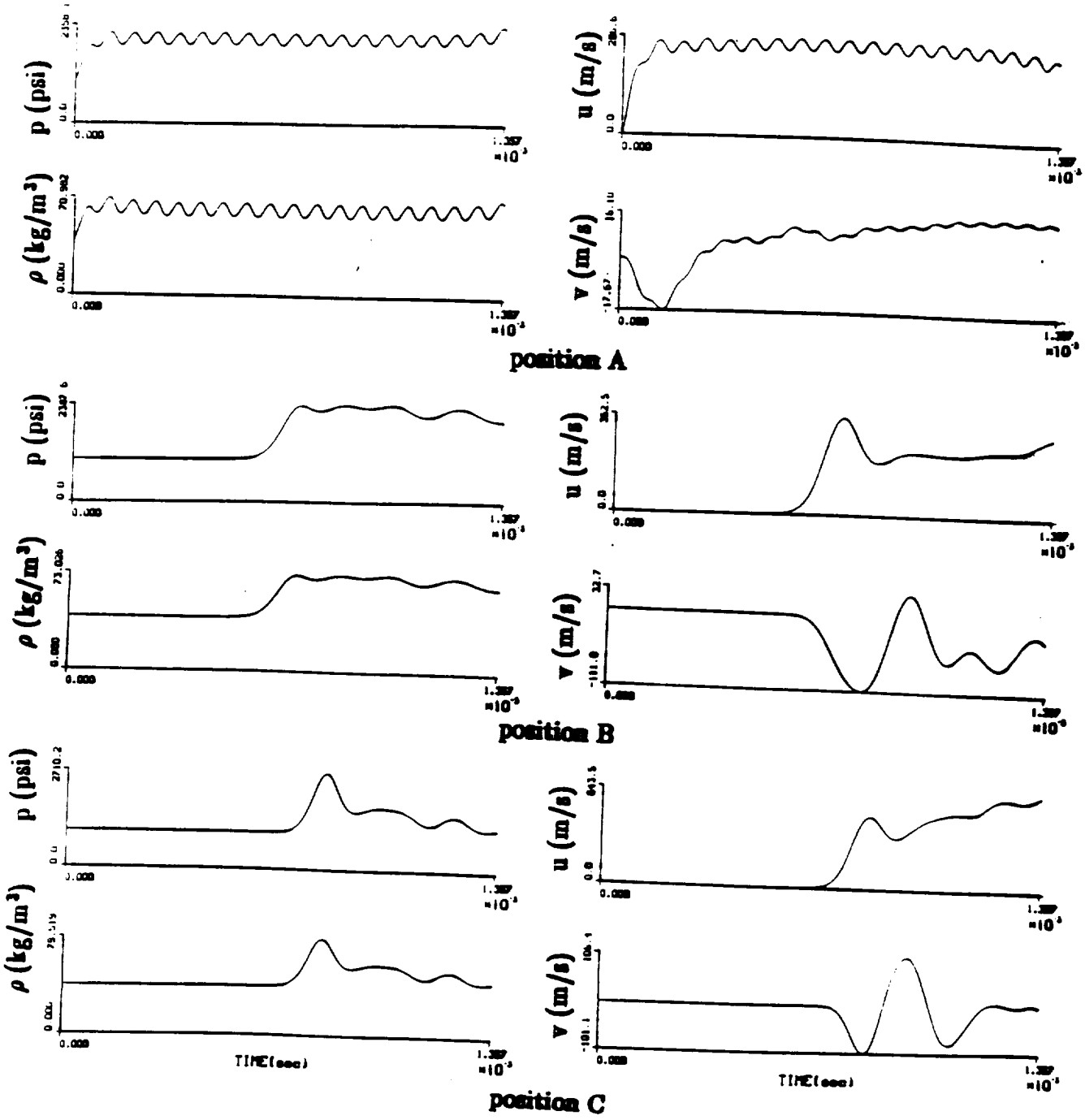

Fig 12 Wave forms for transient chemically reacting flow with disturbances, pressure, density, axial velocity and radial velocity vs time at various positions. Position A (1.8, 11.43 cm), Position B (31.75, 11.45 cm), Position C (63.5, 6.55 cm)

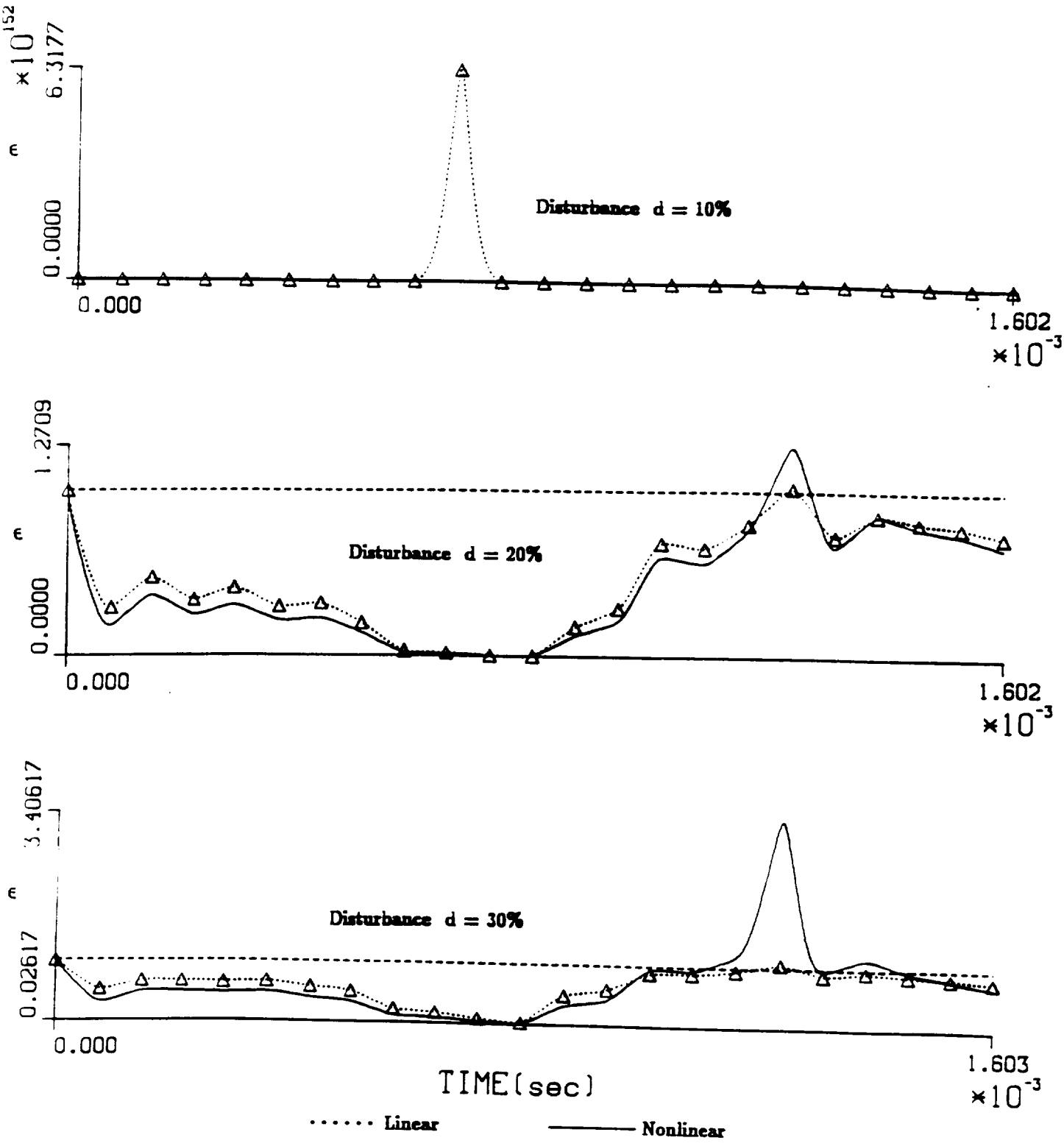

Fig 13 Energy growth factor vs time, transient chemically reacting laminar flow with disturbances, $\bar{p}$ = 500 psi, f (inlet) = 5583 Hz, inlet velocity = 500 m/s

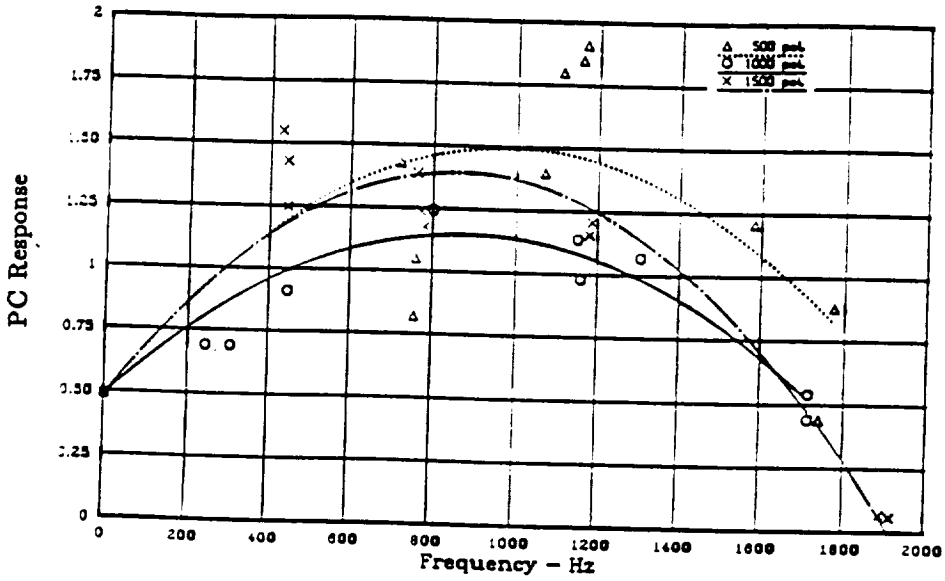

Fig 14 NWC response function measurement, Reference 15, used for determination of burning surface normal velocity

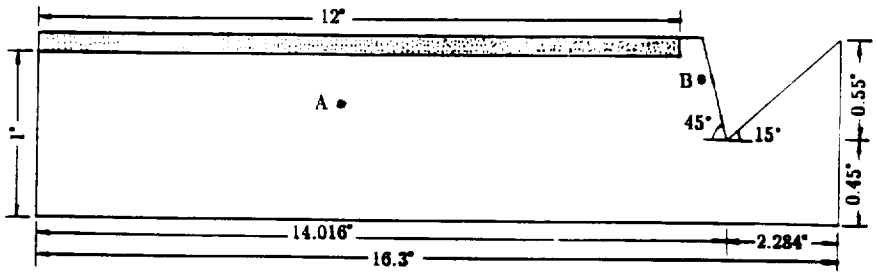

Fig 15 **Motor geometry for stability calculations, A (x = 5.49", y = 0.79"), B (x = 13", y = 0.84")**

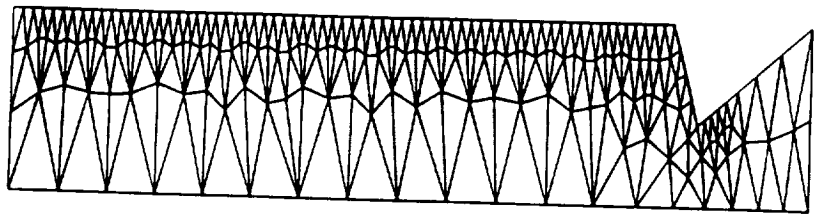

Fig 16a **Finite element intermediate adaptive mesh configuration, 332 elements, 219 nodes**

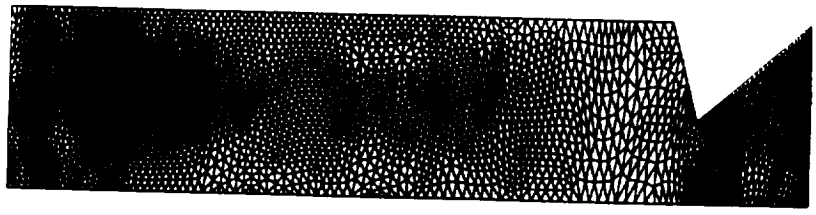

Fig 16b **Finite element final adaptive mesh configuration, 4040 elements, 2159 nodes**

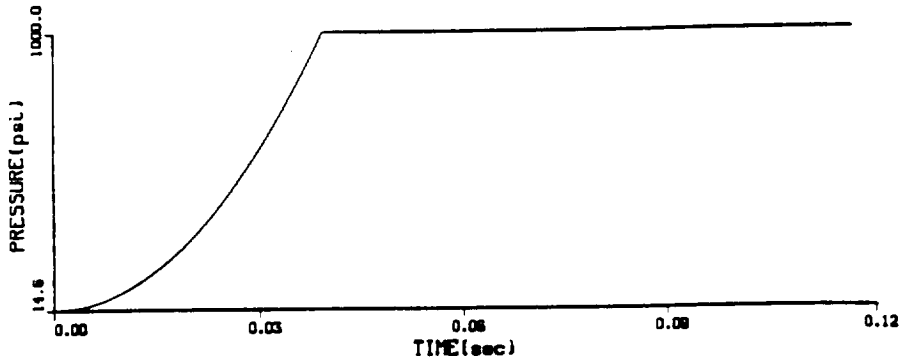

Fig 17a **Burning surface mean pressure $\bar{p}$, oscillatory motion modeled by $p' = \bar{p}\,(1 + d \sin \omega t)$, d = percent disturbance, ω = driving frequency**

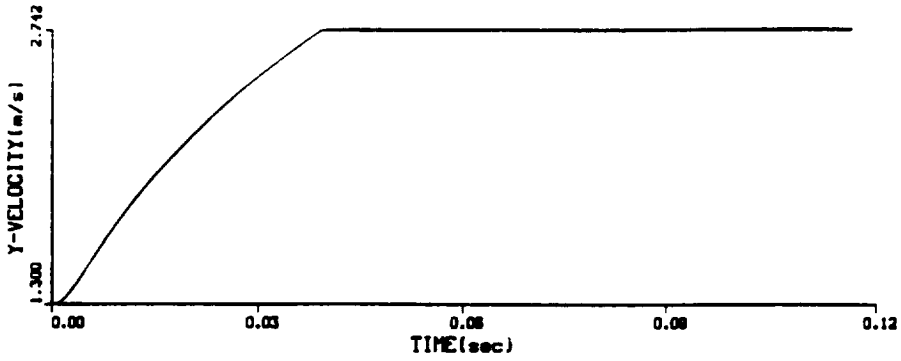

Fig 17b **Burning surface mean velocity $\bar{v}$, oscillatory motion calculated from response function**

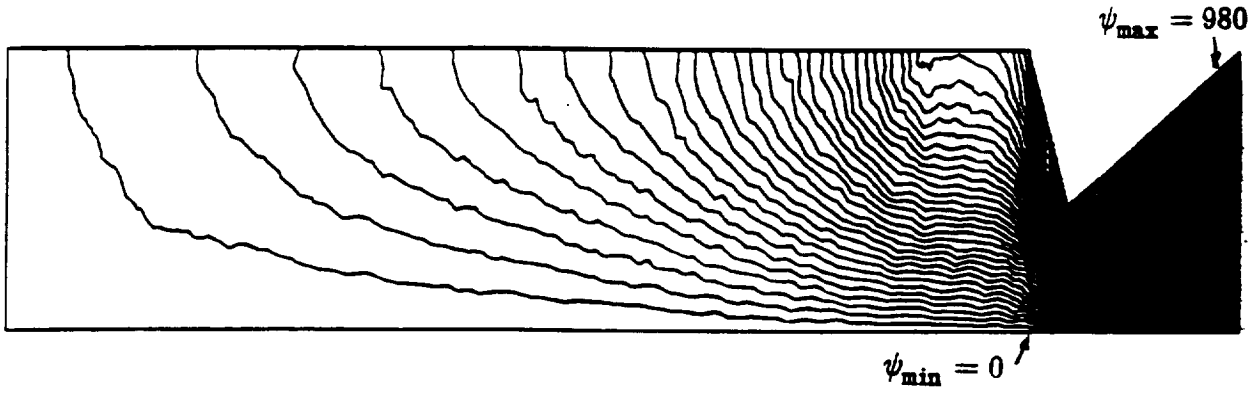

Fig 18 **Streamline contours, minimum $\psi = 0$, maximum $\psi = 980$ with $\Delta\psi = 2.8$**

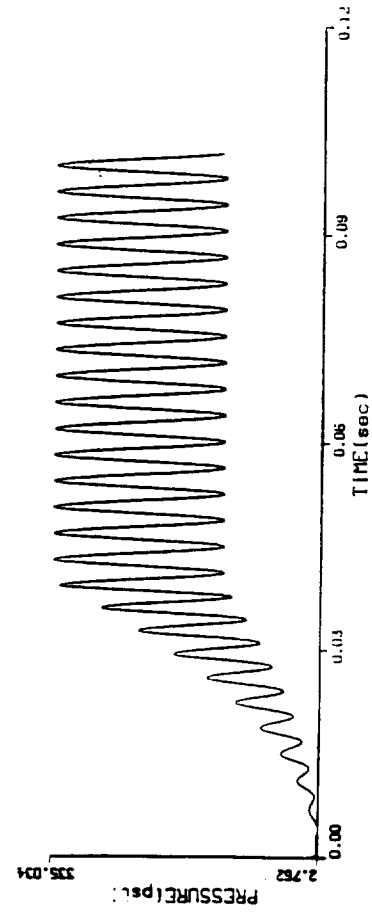

(c) d = 50%

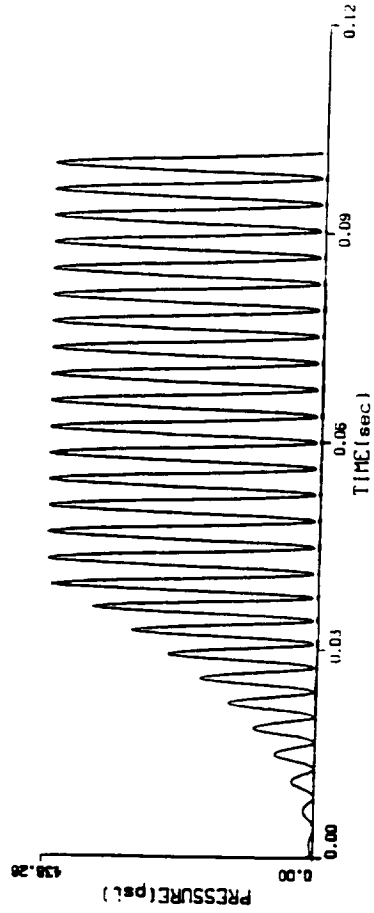

(d) d = 80%

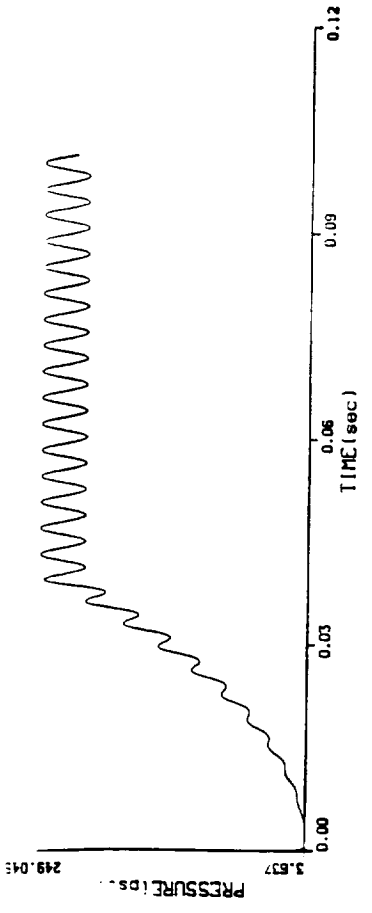

(a) d = 10%

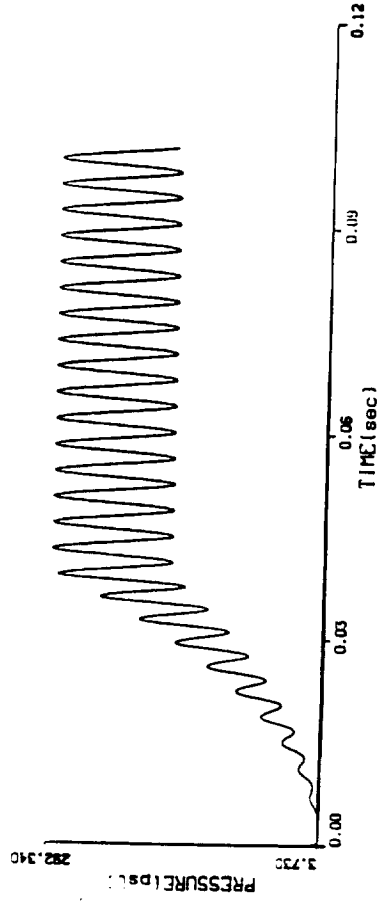

(b) d = 30%

Fig 19 Pressure waveforms at location A for various % disturbances

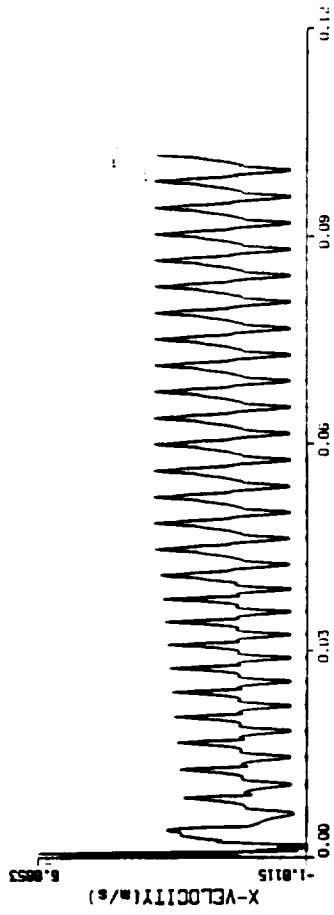

(c) d = 50%

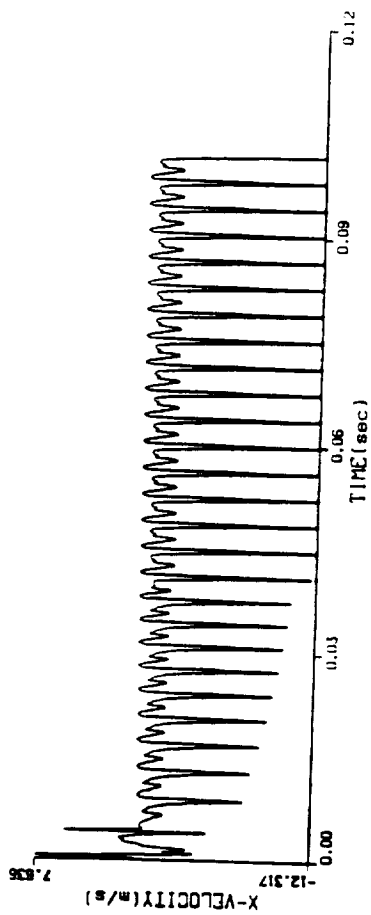

(d) d = 80%

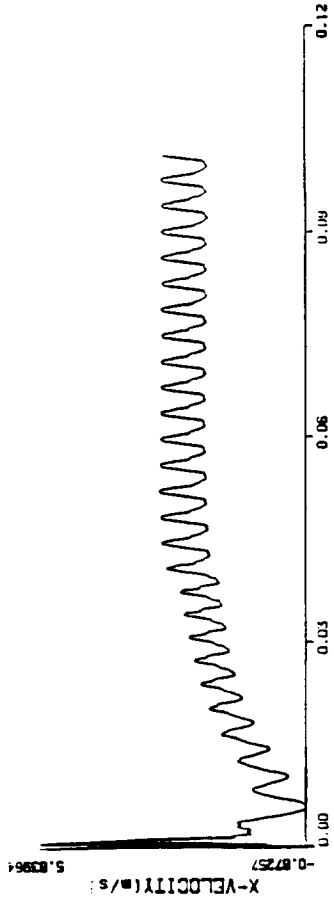

(a) d = 10%

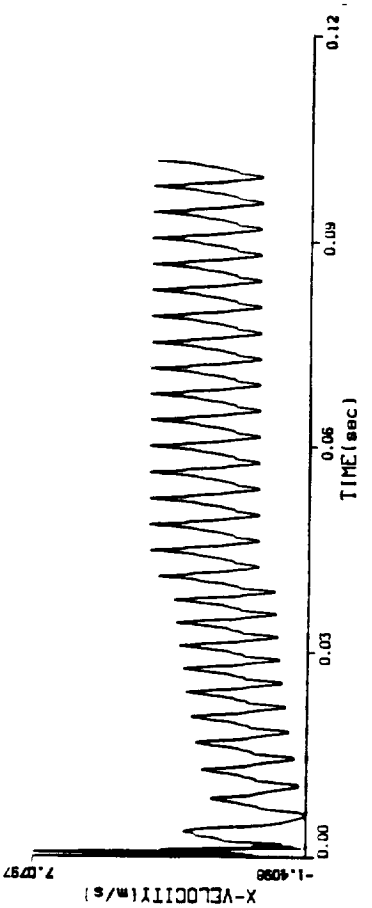

(b) d = 30%

Fig 20 Longitudinal velocity waveforms at location A for various % disturbances

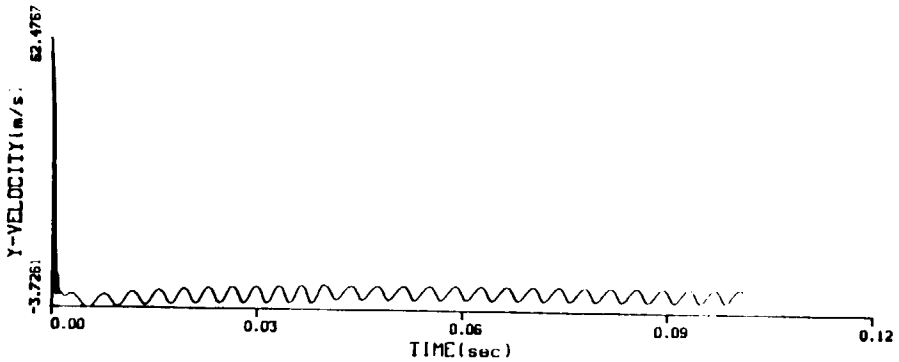

(a) d = 10%

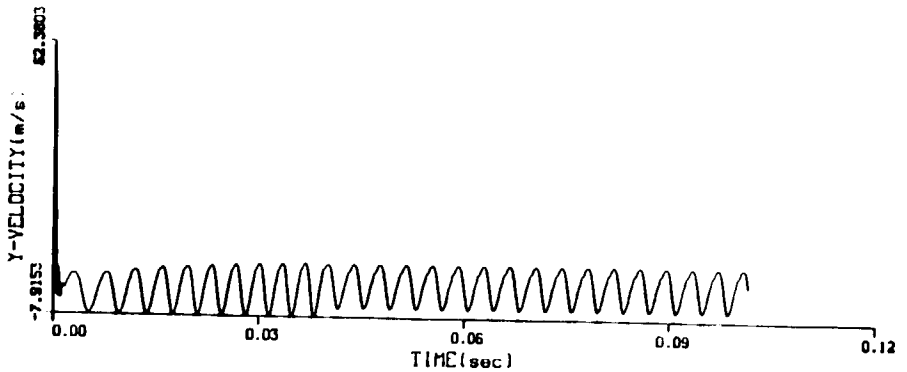

(b) d = 30%

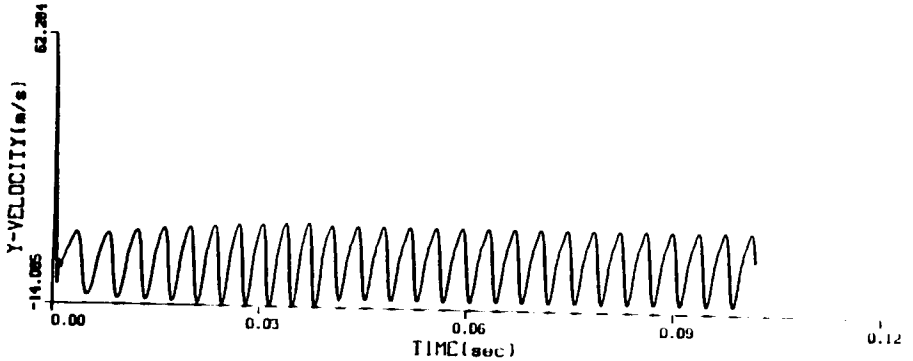

(c) d = 50%

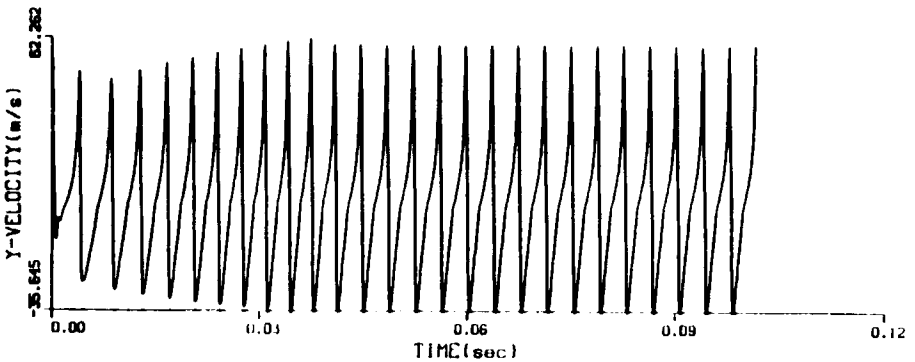

(d) d = 80%

Fig 21 **Radial velocity waveforms at location A for various % disturbances**

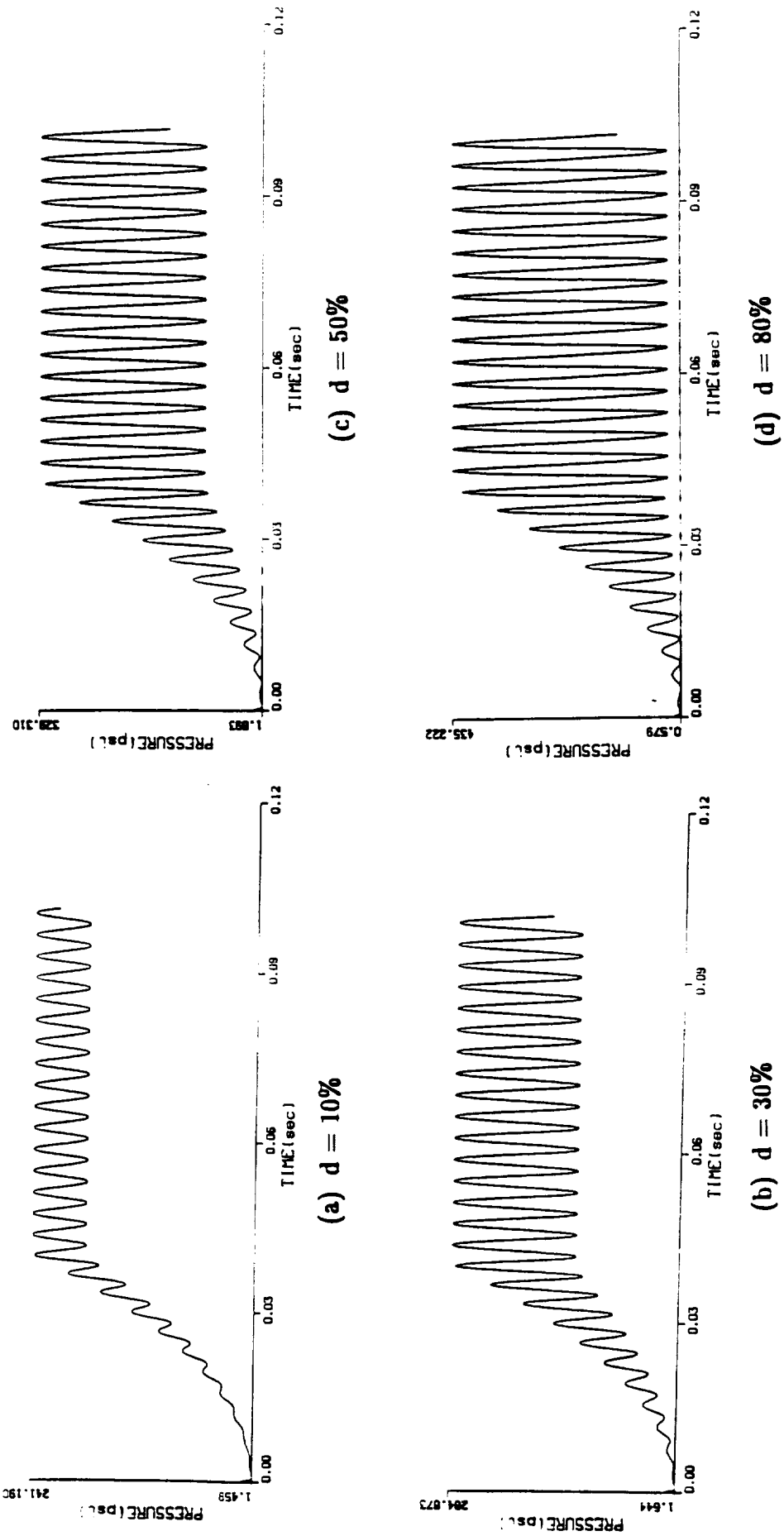

Fig 22 Pressure waveforms at location B for various % disturbances

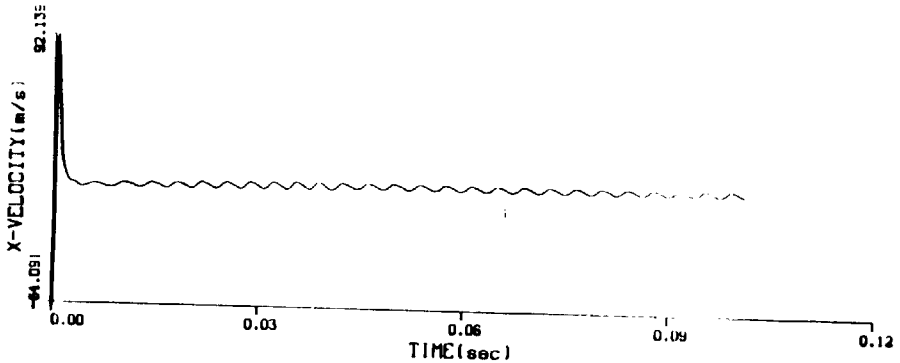

(a) d = 10%

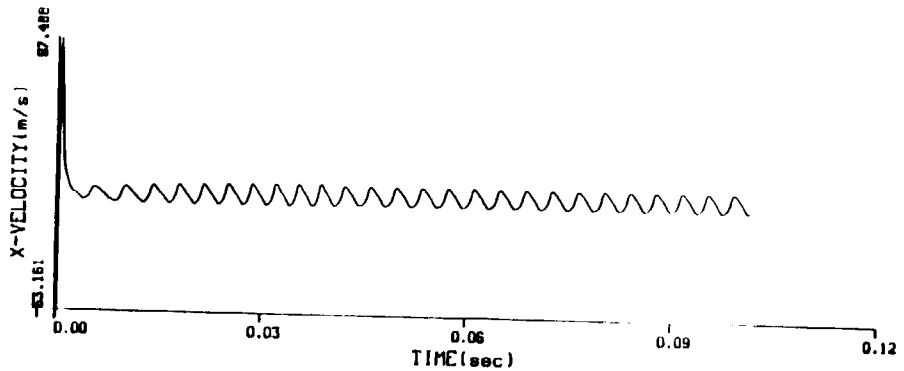

(b) d = 30%

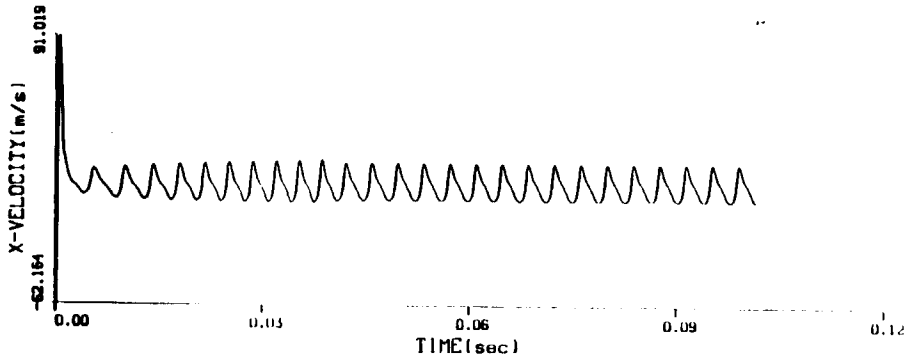

(c) d = 50%

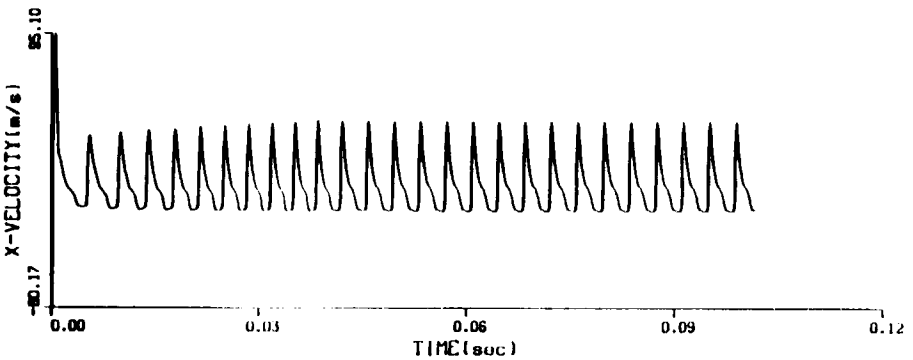

(d) d = 80%

Fig 23 Longitudinal velocity waveforms at location B for various % disturbances

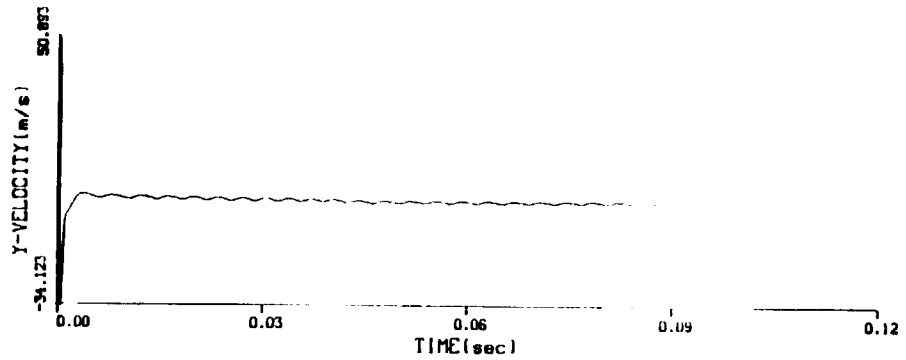

(a) d = 10%

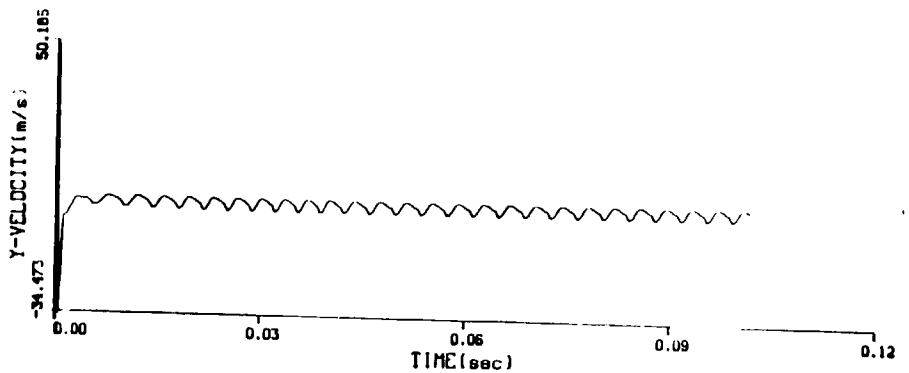

(b) d = 30%

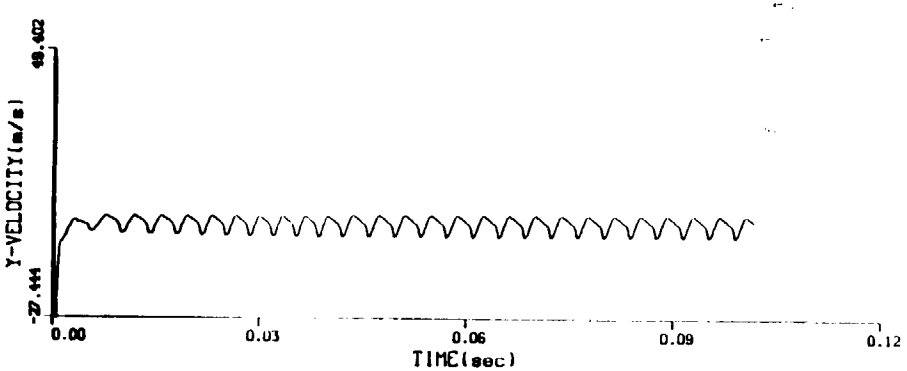

(c) d = 50%

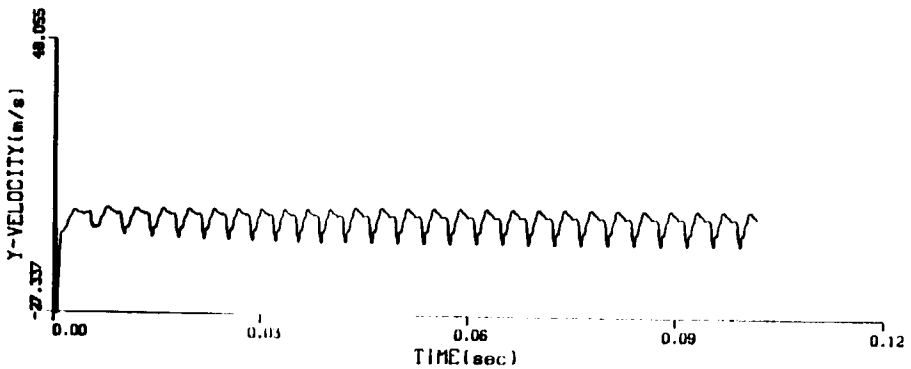

(d) d = 80%

Fig 24 Radial velocity waveforms at location B for various % disturbances

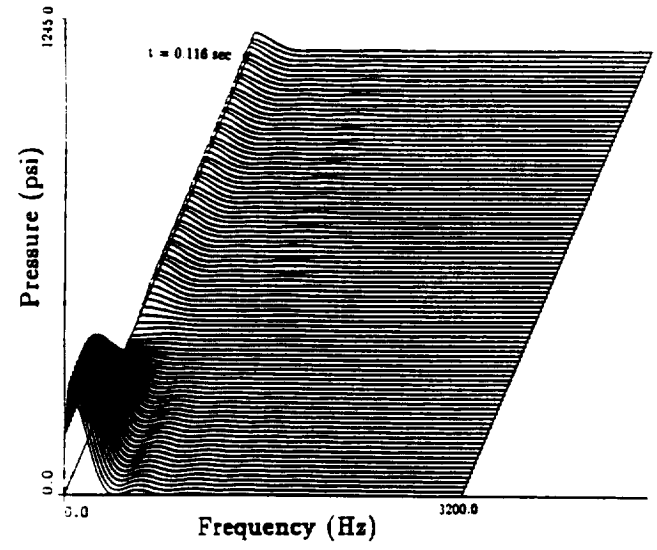

(a) d = 10%

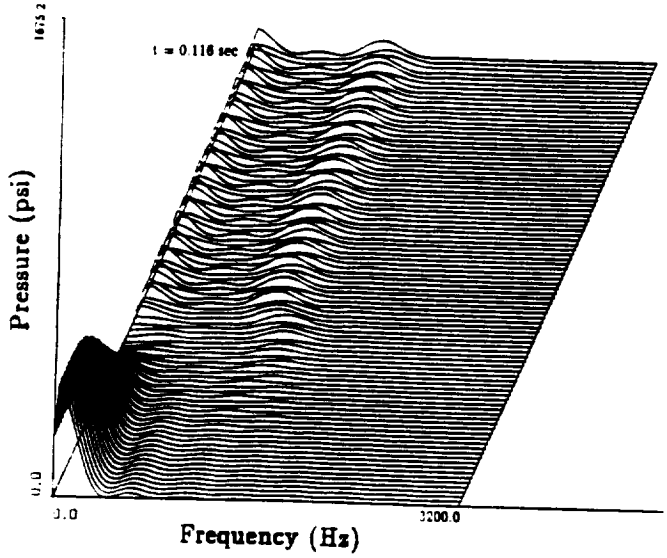

(c) d = 50%

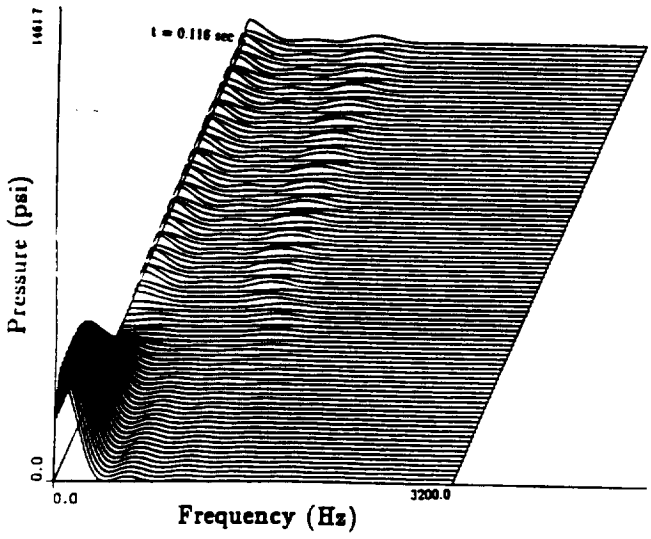

(b) d = 30%

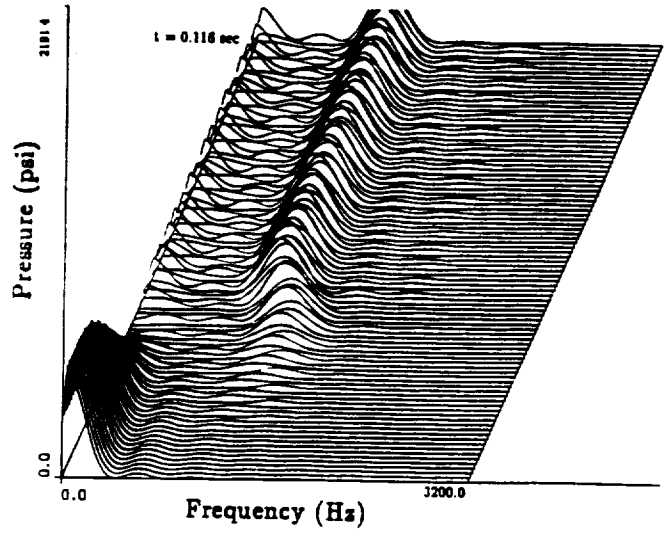

(d) d = 80%

Fig 25 **Waterfall plots for pressure at location A for various % disturbances**

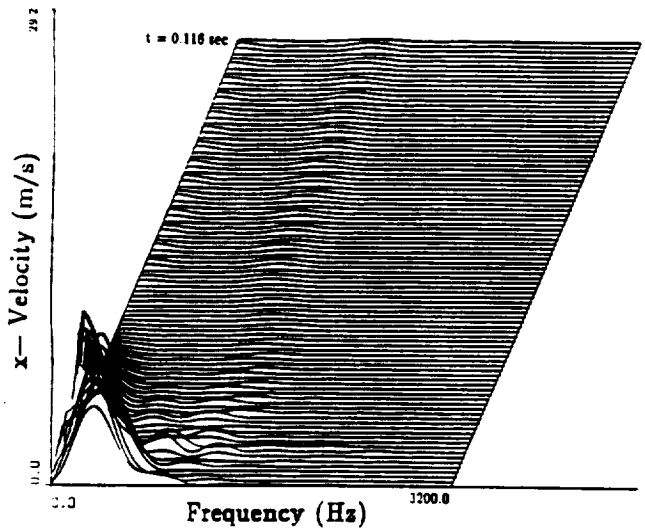

(a) d = 10%

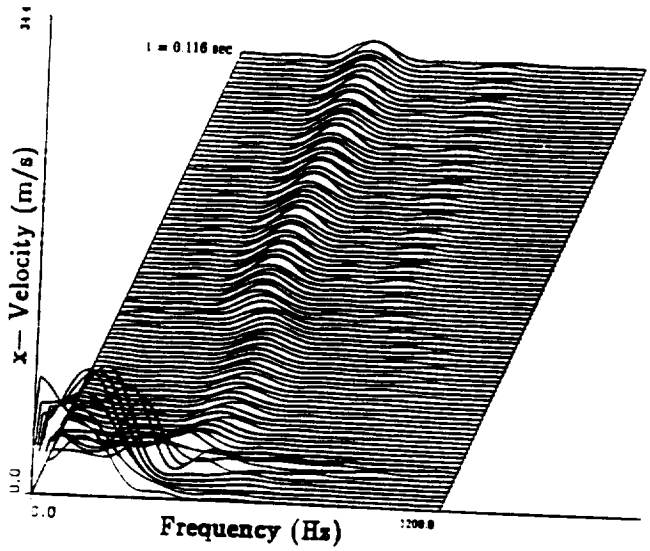

(c) d = 50%

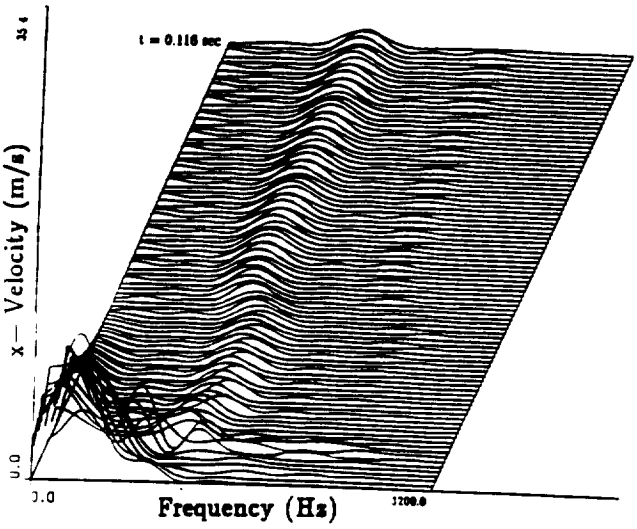

(b) d = 30%

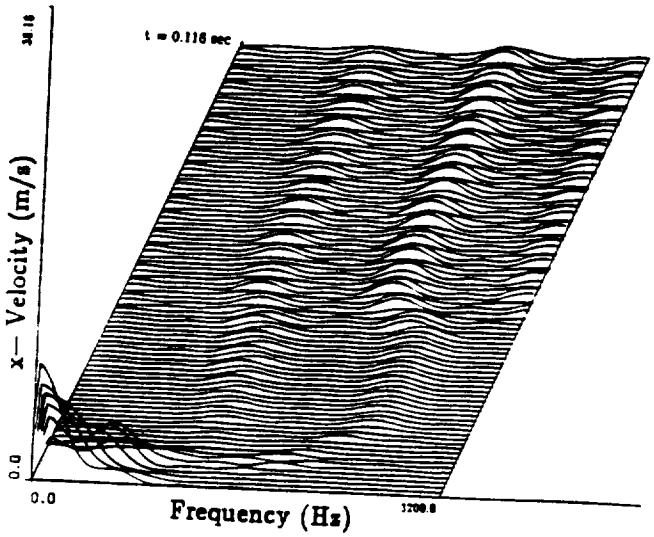

(d) d = 80%

Fig 26 **Waterfall plots for longitudinal velocity at location A for various % disturbances**

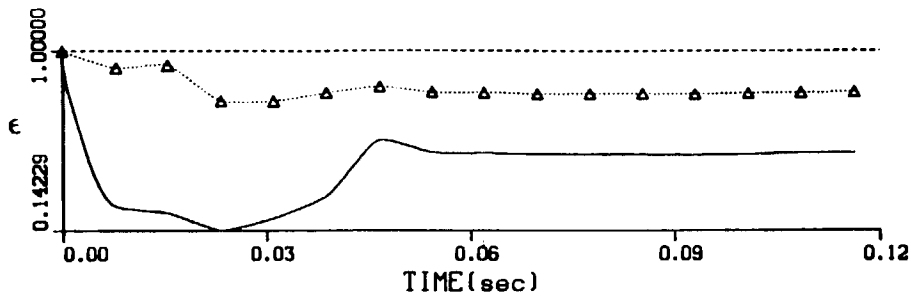

(a) d = 10%

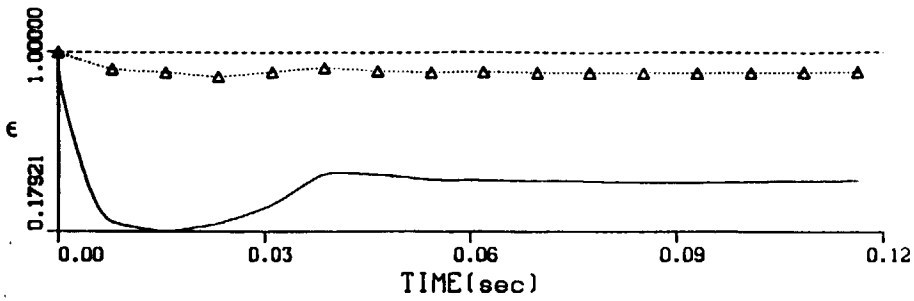

(c) d = 50%

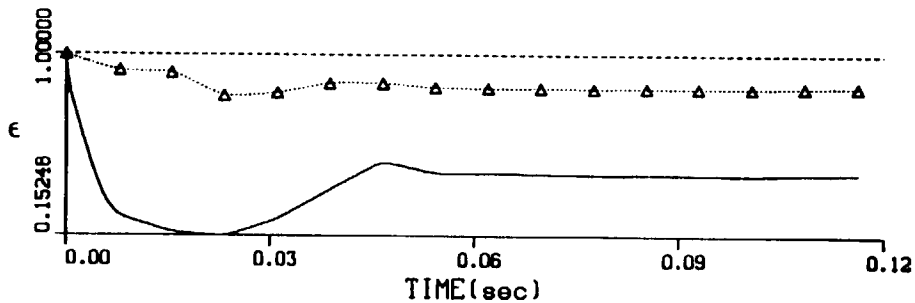

(b) d = 30%

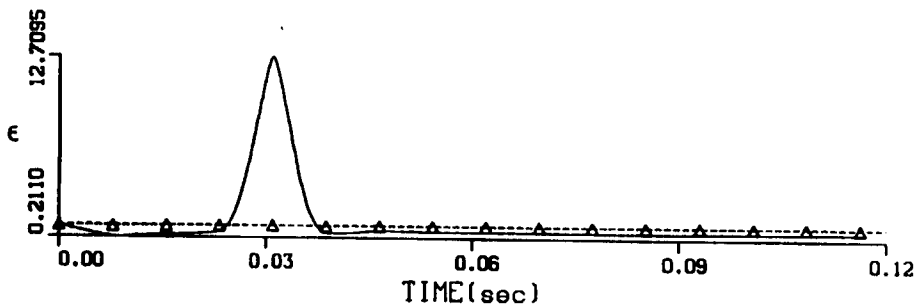

(d) d = 80%

····· Linear ——— Nonlinear

Fig 27 **Energy growth factors for various % disturbances**